Hysteresis and dichotomous mechanics in cyclic crushing failure of confined freshwater columnar ice
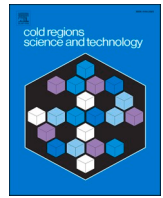
Owen, Cody C.; Hammer, Tim C.; Hendrikse, Hayo

Important note
To cite this publication, please use the final published version (if applicable).
Please check the document version above.

Hysteresis and dichotomous mechanics in cyclic crushing failure of confined freshwater columnar ice

Cody C. Owen [*], Tim C. Hammer, Hayo Hendrikse

Department of Hydraulic Engineering, Delft University of Technology, Delft, the Netherlands

A B S T R A C T

Cyclic crushing experiments with a haversine velocity waveform were performed on passively confined, freshwater columnar ice specimens for a variety of velocities and frequencies. The aim of the experiments was to study the ice deformation and failure behavior in crushing when loaded at a predefined displacement pattern closely resembling the frequency lock-in regime of ice-induced vibrations. The focus of the experiments was on the development of load and ice deformation behavior at the grain and ice specimen scales during each cycle. To this end, the deformation and failure of the ice were observed with crossed-polarized light to highlight the microstructure in-situ during cyclic crushing. It was shown that there are dichotomous mechanical behaviors of the damaged and confined ice during a single crushing cycle: brittle at high velocity and non-brittle at low velocity. At low velocity, ice fracture was interrupted and stress relaxation occurred until the predefined velocity began increasing in the cycle. The stress relaxation in the load was accompanied by stress-optic effects in the ice. It was found that a load peak-velocity hysteresis developed in each crushing cycle: peak loads following the non-brittle behavior were temporarily higher than the peak loads of the brittle behavior. The temporary load peak enhancement tended to increase with increasing duration of stress relaxation, i.e. the peak enhancement tended to increase with decreasing velocity and frequency. Negligible peak enhancement and stress relaxation duration were observed for the highest frequency and mean velocity tested of 2 Hz and 10 mm s^{-1}, respectively. For tests with a minimum velocity of 1 mm s^{-1}, no stress relaxation was observed in the load measurement. Preliminary results from deviating from the haversine velocity waveform by increasing the minimum velocity showed that the stress relaxation duration decreases, but the non-brittle peak load does not decrease. It is speculated that ice anelastic ice behavior could account for the rapid stress relaxation at low velocity. It is unclear what causes the hysteresis, although it is speculated that dynamic strain aging might play a role. The change in ice behavior during the experiments demonstrates a mechanism which develops rapidly and might therefore incite the development of the frequency lock-in regime of ice-induced vibrations of vertically-sided structures.

1. Introduction

For the design of vertically-sided offshore structures—such as offshore wind turbines on monopile foundations—in cold regions, the scenario must be considered in which a drifting ice floe fails in crushing against the structure (International Standard Organization, 2019). If the structure is sufficiently compliant at the ice action point, then the phenomenon known as ice-induced vibrations can develop. Depending on the ice drift speed and the ice thickness, among other factors, severe vibrations can develop which interfere with operability, cause fatigue damage, or even lead to failure of the structure (Björk, 1981). Therefore,

accurate prediction of the development of ice-induced vibrations is important in the design of these offshore structures. Numerical modeling of dynamic ice-structure interaction serves the purpose of predicting the development of ice-induced vibrations, and requires full-scale measurements for validation. Some data exist for navigational aids (Kärnä et al., 2001; Schwarz, 1994) and hydrocarbon platforms (Jefferies and Wright, 1988), but not for offshore wind turbines. To remedy this dearth of full-scale data, model-scale experiments have been performed and a scaling approach is suggested which provide a benchmark dataset for dynamic ice-structure interaction of offshore wind turbine support structures (Hammer et al., 2023). However, even with these data,

accurate prediction of the development of ice-induced vibrations is limited because a governing physical mechanism remains obscure. Moreover, current dynamic ice-structure interaction models are phenomenological in implementation and applicable only for structures and ice conditions which are similar to a given reference case (Hendrikse and Nord, 2019; Kärnä et al., 1999). Therefore, better understanding of ice deformation and failure behavior during ice-induced vibrations is sought to improve the accuracy in prediction of the development of ice-induced vibrations.

A physical mechanism governing ice-induced vibrations, and specifically frequency lock-in, has remained in debate ever since such vibrations were observed in Cook Inlet, Alaska (Peyton, 1968). Historically, the theories of 1) characteristic ice failure length or frequency, and 2) negative damping-based self-excitation were proposed to explain the perpetuation of severe structural vibrations (Määttänen, 1988; Sodhi, 1988). However, model-scale experimental observations of ice loads identified from a rigid pile showed that no distinct characteristic ice failure frequency occurred; instead, a distribution of frequencies developed with a median that increases with increasing ice drift speed (van den Berg et al., 2022). Furthermore, the negative damping theory relies on an ice strength dependence which decreases with increasing strain or loading rate, a dependence which was neither universally observed (Cole, 2021; Hendrikse and Metrikine, 2015) nor accounted for the stochastic nature of strength in brittle failure from uniaxial compression and penetration at high strain rates (Jones, 2007; Timco, 1987).

The ductile-to-brittle transitional behavior, namely competition between creep and fracture (Schulson, 1990), of ice with respect to strain rate has been employed to describe the change in deformation and failure behavior of ice at different deformation rates in dynamic ice-structure interaction (Sodhi, 2001; Sodhi and Haehnel, 2003). Additionally, competition between fracture at different scales and dynamic recrystallization in high-pressure zones at the ice-structure interface has been suggested as a mechanism governing the dynamic loading in ice-structure interaction (Jordaan et al., 2016; Jordaan, 2001). But neither creep nor fracture nor dynamic recrystallization as discussed in literature have been demonstrated to contribute to a governing mechanism in ice-induced vibrations. Consequently, no model based on these ice mechanics has been formulated which accurately predicts the development of frequency lock-in for various structures and ice conditions.

Results from model-scale ice penetration experiments with controlled harmonic oscillation of a pile instrumented with tactile sensors have been interpreted as having an effect of contact area variation on the load level and a delay of global ice failure during a crushing cycle (Hendrikse and Metrikine, 2016). It was found that higher peak loads resulted from longer delay of global ice failure, which were initiated by periods of low relative velocity between ice and pile. But because neither the strain nor the internal deformational behavior of the ice sheet could be measured in the edge indentation tests, a test setup—inspired by the confined ice crushing experiments by Gagnon and Bugden (2008)—was made to investigate the deformation and failure behavior of ice in-situ when crushed while viewing the ice in crossed-polarized light (Owen et al., 2022). By viewing the ice in-situ with crossed-polarized light, it could be verified whether and how dynamic recrystallization manifested during ice-induced vibrations. Emphasis was placed on studying the deformation and failure behavior of full-scale or 'real' ice due to the uncertainty regarding the scalability of model-scale ice properties in the context of ice-induced vibrations of vertically sided structures (Gagnon, 2022).

The following research question is posed: how does the deformation and failure behavior of columnar ice develop during frequency lock-in vibrations? The objective of the present study was to attempt to reproduce the stress and strain states of the ice sheet edge during frequency lock-in vibrations in a small laboratory setting and to observe the ice mechanics involved in the interaction at the grain scale.

To this end, the present study used the aforesaid test setup to apply a haversine displacement rate waveform to a passively-confined, fresh-water columnar ice specimen while being filmed in crossed-polarized transmitted light. Load and velocity time series are presented with video frames, and statistical summaries are provided to illustrate trends in the results. It is shown that there are dichotomous mechanical behaviors of the damaged and confined ice during a single crushing cycle: brittle at high velocity and non-brittle at low velocity. At low velocity, ice fracture is interrupted and stress relaxation occurred until the velocity began increasing in the cycle. The stress relaxation in the load is accompanied by stress-optic effects in the ice. It is found that a load peak-velocity hysteresis developed in each crushing cycle: peak loads following the non-brittle behavior are temporarily higher than the peak loads of the brittle behavior. The temporary load peak enhancement tended to increase with increasing duration of stress relaxation, i.e. the peak enhancement tended to increase with decreasing velocity and frequency. Negligible peak enhancement was observed for the highest frequency and velocity tested. Preliminary results of deviating from the haversine velocity waveform by increasing the minimum velocity showed that the stress relaxation duration decreases, but the non-brittle peak load does not decrease. The results are then compared with load and velocity time histories from model-scale ice tank tests (Hendrikse et al., 2022) with controlled-oscillation of a rigid pile to demonstrate consistency of the observations for different ice types and loading scenarios. Finally, a contribution to a physical mechanism is speculated by comparing both the results of the present study and the ice tank tests to studies establishing anelastic—defined as delayed- or visco-elastic (Cole, 2001)—behavior of ice.

The present study demonstrates novelty in two aspects. First, the application of a haversine velocity waveform—with velocities spanning several orders of magnitude during a cycle—to passively-confined columnar ice resulting in cyclic compressive failure was unique. Second, the observation of the confined ice in-situ with crossed-polarized transmitted light, highlighting deformation and failure at the grain scale, has not been reported previously. In-situ observation of confined ice with crossed-polarized transmitted light was performed only at strain rates and with ice types relevant for glaciological research (Peternell et al., 2011).

The present study is structured in the following manner. The ice preparation, test setup, and experimental procedure are introduced in Section 2. Section 3 summarizes the general observations from the time series and videos. In Section 4, the results of the experiments are elaborated, with specific focus on two particular tests to highlight certain features which can be generalized to the experiments. The two tests consider the effect of 1) the haversine velocity waveform on the load signal, and 2) deviation from the haversine on the load signal. The discussion is given in Section 5 which relates the results from the present study to research on model-scale dynamic ice-structure interaction experiments and ice anelasticity. Finally, the conclusions are presented in Section 6.

2. Experimental setup and procedure

The ice preparation and the "Optical apparatus with Linear Actuator loading Frame" (OLAF) test setup are described by Owen et al. (2022), but additional features have been added and are summarized here.

2.1. Ice preparation

The ice used in the experiments was grown in the ice laboratory using tap water from Delft, Netherlands. The procedure for growing the ice was as follows. First, tap water at room temperature (about 20 °C) was poured into a cooler with dimensions of approximately 430 mm by 400 mm by 320 mm (length by width by depth, Dometic Cool-Ice CI 55, Dometic Group AB, Solna, Sweden) in the cold room which was retrofitted with a heated pressure relief system and ball valve at the base for

emptying the water when desired. The cold room temperature was set at −20 °C and the water surface was left to freeze. Once a thin skim of ice formed, the ice was removed and an internally-dimensioned 200 mm cubic wooden frame was floated in the water to act as the mold for the shape and size of the ice block desired (see Fig. 1). Inside the frame was placed either 1) crushed ice or snow sprinkled onto the surface as dry seeding; or 2) a thin ice plate cut from another ice block to act as a template seed from which the ice grain structure would follow during growth (Barrette et al., 1993). The freezing process in the cooler was mainly unidirectional from the surface of the water due to the insulation from the walls and bottom of the cooler. The unidirectional cooling and the seeding process promoted columnar grain growth. The ice was left to grow for about 72 h; it was found that roughly 80 mm of ice forms in 24 h with this setup. After, for example, 72 h, roughly 185 mm of ice would have grown following the wooden frame, leaving an ideally-shaped cubic ice block nominally free from air pockets or other optical impurities. The remaining water in the cooler was drained via the ball valve and the wooden frame with ice block was cut from the surrounding ice in the cooler.

Once removed from the cooler, the wooden frame and ice block were left at room temperature of about 20 °C to thaw until the ice block separated from the wooden frame. The ice block was then cooled and cut into vertical plates of about 15 mm thickness with a band saw. Each ice plate was welded to an acrylic plate of similar size with warm tap water. While using warm water melts the bottom surface of the plate slightly, the ice that forms generally follows the grain structure of the ice plate and reduces the likelihood of grain growth emanating from the acrylic plate instead. Once welded to the acrylic, the ice plate was milled flat with a computer numerical control (CNC) milling machine. The acrylic plate was then heated so that the ice could be removed and the machined side was welded to the acrylic. Prior to welding, the machined side was heated with a hair dryer to melt the milling grooves and lines and promote a smoother surface for welding. Once the machined side was welded to the acrylic, the specimen was machined a target thickness of 5.20 mm with a machining tolerance of ±0.20 mm over 185 mm and an accuracy of 0.05 mm. The ice thick section was then removed from
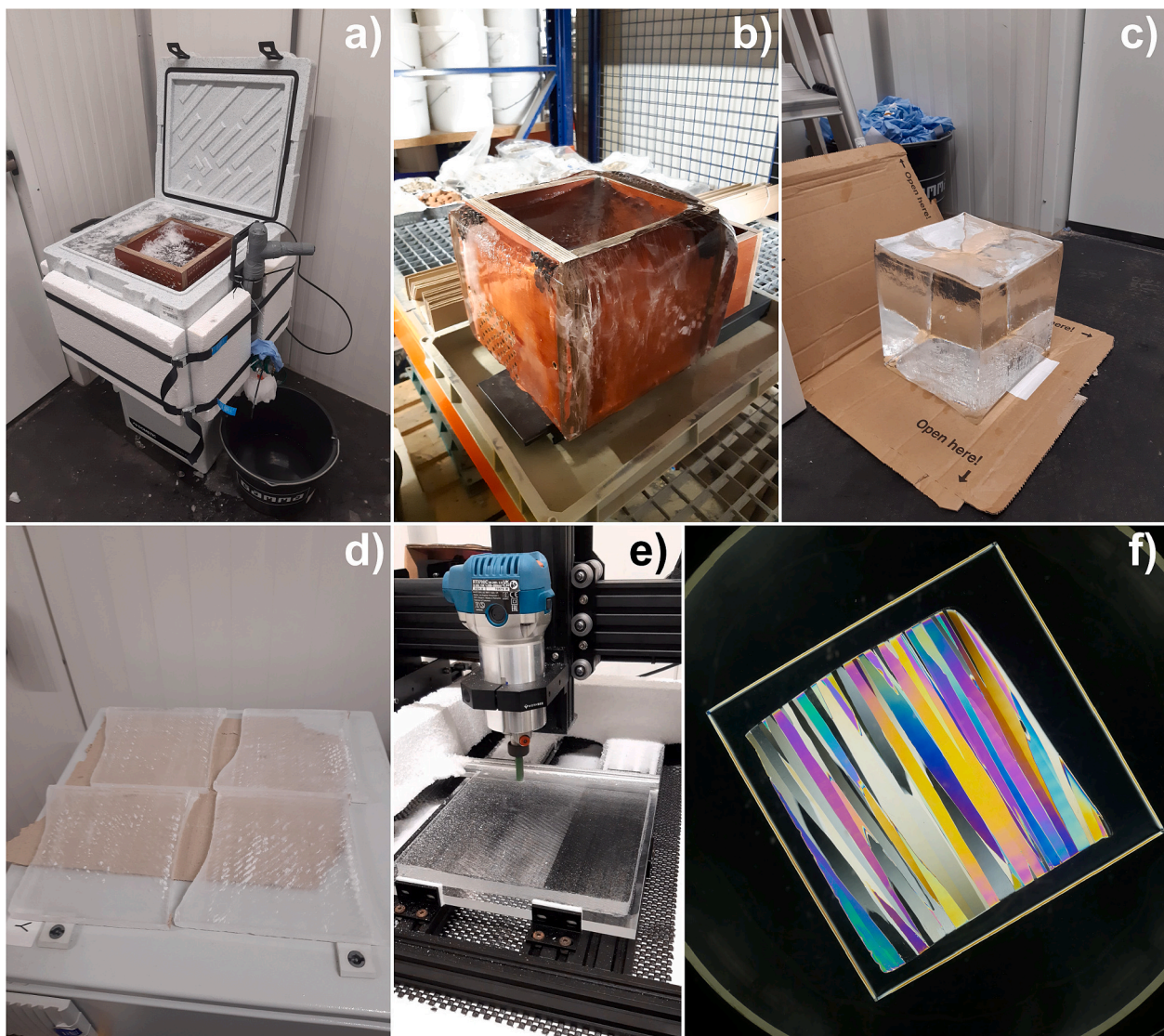

Fig. 1. Photographic summary of the ice preparation process and assessment of grain structure: a) The retrofitted cooler with ice growth within the wooden frame. b) The wooden frame and ice block removed from the cooler and placed outside the cold room to separate the ice from the wood. c) The ice block removed from the wooden frame and placed in the cold room to cool. For this ice block, some air bubbles can be seen within the bottom few centimeters. d) The ice plates cut from the block with a band saw. e) The ice plate, welded to an acrylic plate, is machined with a CNC milling machine. f) An example thin section made from an ice plate and viewed in crossed-polarized transmitted light to assess the grain structure. Note that the photographs are representative and do not necessarily pertain to the same process of the ice preparation.

the acrylic and the machined surface was heated with the aforesaid method, and then the uneven edges from the welding were melted flat. The ice specimen was then ready to be installed in the confinement box as explained next.

2.2. Experimental setup

The OLAF test setup consists of a self-contained load frame with an electric linear actuator (GSX50-1005-MKR-SB5- 358-G2ACTUATION DIVISION-EXLAR Corporation, Eden Prairie MN 55346, USA) which drives a stainless steel indentor plate into a confinement box containing the ice specimen (see Fig. 2). Each ice specimen, a vertical thick section of columnar freshwater ice with approximate dimensions of 185 mm by 185 mm by 5 mm, was passively confined by the confinement box and loaded on the edge by the indentor plate (see Fig. 2b). Specifically, the ice was 1) confined by 40 mm-thick fused-silica glass plates orthogonal to the light source; 2) confined opposite the indentor plate by the steel backing plate in the direction of loading; and 3) confined by acrylic plates which were frozen in place in the aft-part of the confinement box

to provide confinement upward and downward in the plane of loading to prevent splitting failure of the ice plate (see Fig. 2c). The ice was free to deform, fracture, and clear upward and downward in the plane of loading in the fore-part of the confinement box, and was otherwise approximately rigidly confined.

The force was measured with a load cell (VST5000 S-type load cell, HENK MAAS Weegschalen B.V., 4264 AW Veen, The Netherlands) between the indentor plate and the linear actuator at 1–2 kHz. The displacement of the indentor plate was measured by a magneto-strictive displacement sensor (BIW0007-BIW1-A310-M0250-P1-S115 Balluff B. V., 5232 BC 's-Hertogenbosch, The Netherlands), also at 1–2 kHz, which was connected to the torque compensation rod of the linear actuator. The ice specimen was filmed at 2.7 K resolution and 50 frames per second with two cameras (GoPro HERO9 Black, 3025 Clearview Way, San Mateo, CA 94402, USA), each at a different angle and distance from the viewing window of the confinement box, in crossed-polarized light (see Fig. 2d). The crossed-polarized light was supplied by an LED light panel (JINBEI EFP-50 BICOLOR LED PANEL LIGHT, RCP Handels-GmbH & Co. KG, in de Tarpen 42, D-22848 Norderstedt, Germany) with a
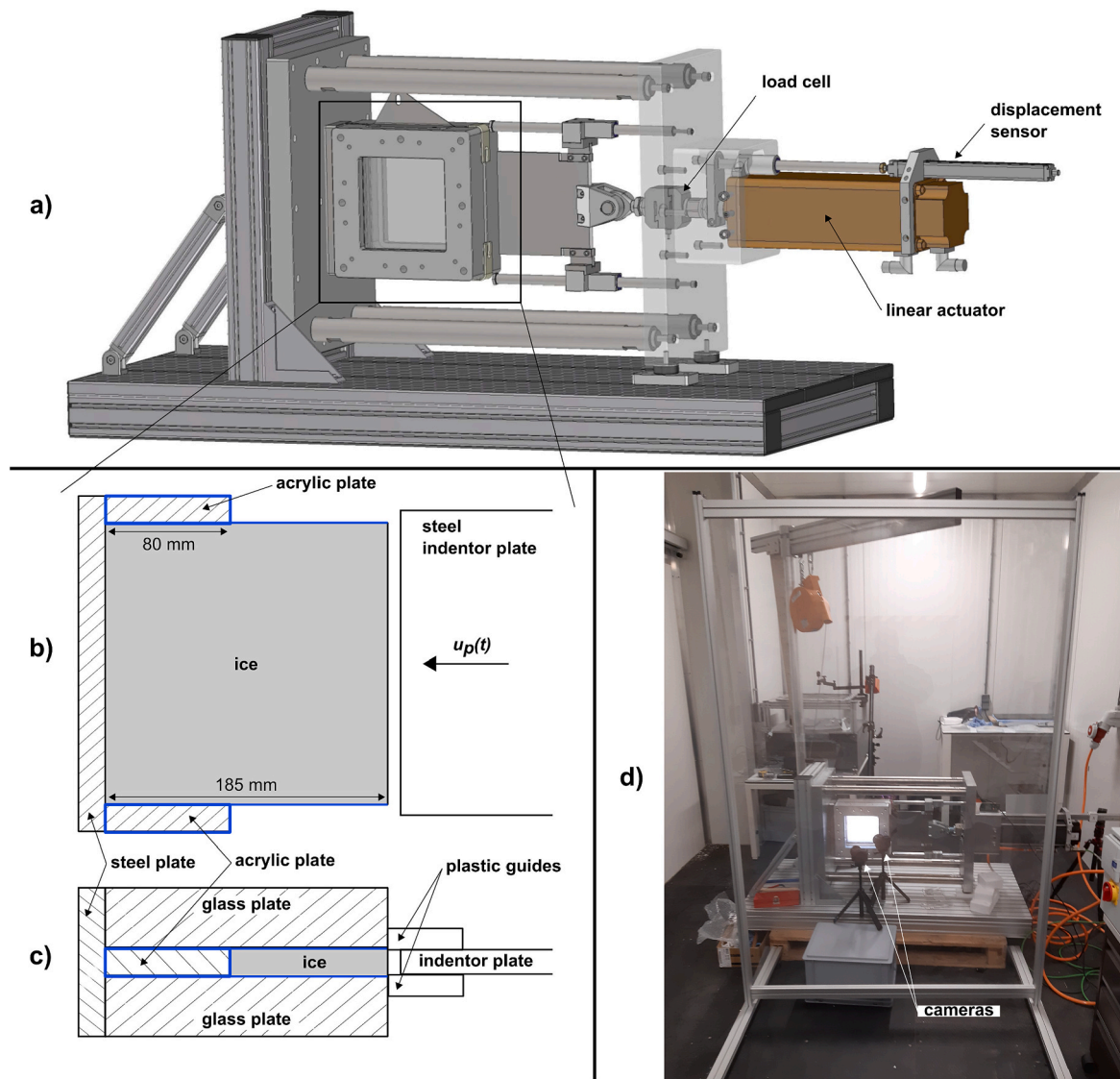

Fig. 2. Visual description of OLAF test setup: a) Schematic of the OLAF test setup (Owen et al., 2022). b) Profile view schematic of ice confinement and crushing scenario. The nominal direction and imposed displacement of the indentor plate are denoted by $u_p(t)$ and are discussed in Section 2.3. c) Top plan view schematic of ice confinement and crushing scenario. Note that the blue lines indicate the locations of weld water added for affixing the acrylic plates and ice specimen to the confinement box. d) Photograph of OLAF in the cold room with cameras mounted on tripods during testing. (For interpretation of the references to color in this figure legend, the reader is referred to the web version of this article.)

linear polarizer. The cameras were fitted with linear polarizers and macro lenses for the short depth of field. All hardware, software, and non-structural equipment were adapted from another test campaign (Hammer et al., 2021; Hendrikse et al., 2022).

2.3. Experimental procedure and test matrix

For level ice drifting with a constant speed and crushing against a compliant offshore structure, structural vibrations may develop which resemble sinusoidal oscillation; this is termed frequency lock-in. During frequency lock-in, the relative velocity between the ice drift and structure oscillates between roughly double the ice drift speed and zero. To emulate this relative velocity pattern with the test setup, the indentor plate followed a haversine velocity waveform $\dot{u}_p$:

$$\dot{u}_p(t) = \overline{v}[1 + \alpha cos(2\pi f t)] \qquad (1)$$

which is the time derivative of a constant displacement rate superimposed with a sinusoidal displacement u_p:

$$u_p(t) = \overline{v}t + \frac{\alpha \overline{v}}{2\pi f} sin(2\pi f t) \qquad (2)$$

where t is time, $\overline{v}$ is the mean velocity, α is a scale factor for the velocity amplitude, f is the controlled frequency of the indentor plate displacement. Example time series of imposed displacement and corresponding velocity of the indentor plate and their relations to $\overline{v}$, f, and α are shown in Fig. 3.

A total of 12 individual tests were performed in which $\overline{v}$, f, and α were varied (see Table 1). The mean velocities ranged from 0.4 to 10 mm s^{-1}, the frequencies from 0.2 to 2 Hz, and the scale factor from 0.5 to 1. The air temperature was $-8 \pm 2\,°C$ for all tests, which was controlled by the refrigeration system of the cold room and locally measured with a digital temperature logger (Extech RHT30 Multi-channel data logger, Teledyne FLIR LLC, USA). The ice temperature was not directly measured, but the ice was equilibrated in the cold room for at least two hours before testing. To ensure full contact between the indentor plate and ice specimen, and improved confinement of the ice plate in the confinement box, pre-straining (deformation of the specimen prior to cyclic crushing) of 0.5% at $2 \cdot 10^{-3}$ mm s^{-1} was performed for all tests. Pre-straining resulted in the formation of some cracks and growth of existing cracks caused accidentally during installation of the ice specimen into the confinement box. Implications of the preexisting cracks are addressed in Section 2.5. The nominal crushing distance for each test was about 40 mm or 20% of the length of the specimen.

Table 1
Test matrix of the cyclic crushing experiments.

Test [#]	Date	$\overline{v}$ [mm s^{-1}]	f [Hz]	α [−]
1	04-07-22	0.4	0.2	1
2	05-07-22	1.0	0.2	1
3	06-07-22	5.0	0.2	1
4	07-07-22	5.0	1.0	1
5	08-07-22	2.0	0.5	1
6	11-07-22	1.0	0.2	0.9
7	12-07-22	5.0	2.0	1
8	15-07-22	10.0	2.0	1
9	18-07-22	1.0	0.2	0.75
10	19-07-22	1.0	0.2	0.5
11	29-09-22	2.0	0.2	1
12	03–10-22	2.0	0.2	0.5

2.4. Method of data post-processing

The displacement measurements were filtered with an 8th order Bessel and zero-phase shift filter to reduce the significant noise from the 50 Hz power source in the data acquisition system. The velocity of the indentor plate was derived from the displacement measurements, which required additional filtering of the same type after the differentiation. The force measurements were not externally filtered. The raw videos from the GoPro cameras were compressed using a H-264 codec. The videos were visually synchronized with the force and displacement signals according the first major fracture event, or a clearer subsequent fracture event that was easily discernable from both the video and force records.

2.5. Impact of test setup on measurements

A large scatter was observed in the mean load which contained uncertainty from differences in passive confinement of the confinement box and differences in contact area during each test. The confinement of the ice by the glass plates was not measured, and complete contact between the ice and glass plates was not guaranteed due to machining limitations for the parallelity of the ice specimen. The contact area was observed to vary significantly during the tests because of the fracture and fragmentation of the intact specimen, though contact area was not directly measured in the experiments. Moreover, cracks were formed during the installation of the ice specimen into the confinement box and acted as nucleation points for fragmentation, which formed differently
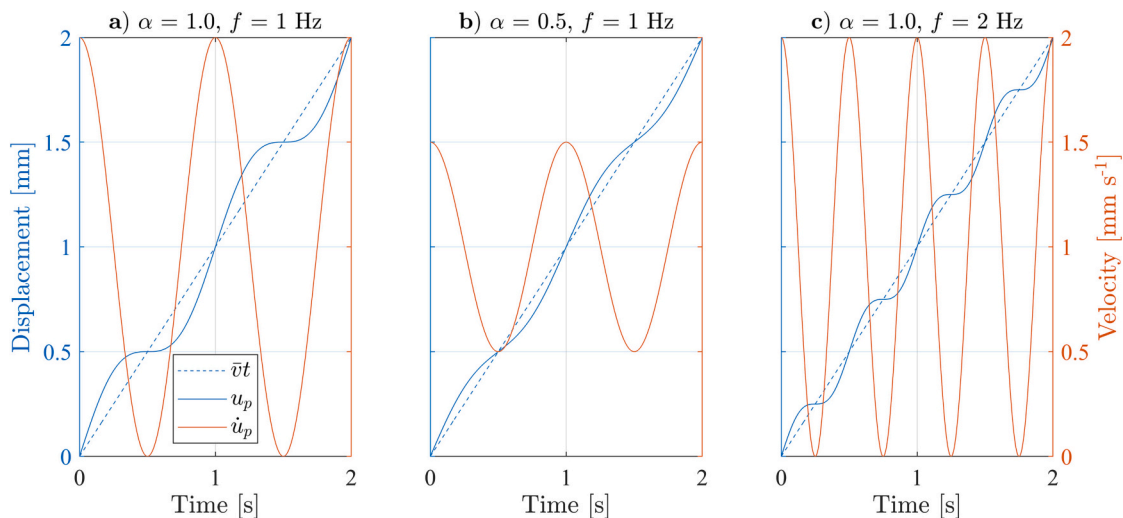

Fig. 3. Example time series of displacement (and corresponding displacement rate, or velocity) waveform used as input to the linear actuator controller. These time series use as input $\overline{v} = 1$ mm s^{-1}, and a) $\alpha = 1$, $f = 1$ Hz; b) $\alpha = 0.5$, $f = 1$ Hz; c) $\alpha = 1$, $f = 2$ Hz.

for each test.

Plastic guides were used to ensure the indentor plate entered the confinement box and maintained alignment within the box (see Fig. 2c). These guides induced frictional forces on the indentor plate of no greater than 0.3 kN, which were not subtracted since these forces were roughly the same across all tests.

It was found that the test setup was not rigid and noticeable vibrations were present in the displacement measurements. This also meant that the derived velocity signals contained vibrations of the test setup after large load drops. However, some of the recorded vibrations were likely noise from the power source, especially where the load signal did not follow these vibrations in the displacement. In cases where load drops were on the order of 1 kN or more, the indentor plate, and the test setup as a whole, underwent transient vibrations which could be clearly observed in the time series and in the videos from the shaking of the cameras. The effect of the lack of stiffness in the test setup on the test results is elaborated in Section 5.1.

3. General observations from experiments

The following general observations from the experiments are supported with results from Test #2 for the sake of brevity. The time series of load and velocity for all tests can be found in the supplementary material. Synchronized videos with the load and velocity time series for all tests, as well as the raw data and post-processing techniques, are publically available and can be found here: https://doi.org/10.4121/22047680.v1.

3.1. Load and motion signals

All tests began with initial contact between the indentor plate and ice, typically followed by elastic loading and subsequent fracturing, consisting of numerous events, of the ice specimen when the velocity was high (see Fig. 4). The brittle crushing failure can be characterized by linear load increases followed by sudden load drops (sawtooth-like load pattern). The first load drop was usually much higher than subsequent load drops due to the greater contact area of the ice specimen at the beginning of the test.

For all tests where $\alpha = 1$ (proper haversine velocity waveform), when the velocity was relatively low and decreasing the brittle failure was interrupted and unloading of the ice specimen was observed, where the load signal became smooth (e.g. see Fig. 5). This period of unloading (Marker 2 to 3 in Fig. 5) was followed by reloading (Marker 3 to 4) when the velocity began increasing and typically a load build-up and fracture

occurred (Marker 4 to 5), where the load prior to failure was higher than the mean of the previous brittle load peaks. This behavior was lost when significant damage developed in the ice specimen, resulting in extrusion. The load from the extrusion process was relatively smooth and low during both low and high velocity in a cycle. Damage of the ice specimen refers to a dense field of cracks without apparent separation of the intact ice into fragments.

For some tests where $\overline{v} \leq 1$ mm s^{-1}, the latter portion of the time series showed little or no sawtooth-like load, especially when the ice specimen became uniformly damaged (see Section 4.5). For these tests, it appeared that the significant, uniformly distributed damage inhibited further ice fracture and instead allowed for extrusion of the damaged material.

3.2. Videos

All individual tests were performed on vertical thick sections of columnar, freshwater ice with mean grain columnar diameters on the order of 10–20 mm and with nominally random orientation of the c-axes perpendicular to the growth direction (see Fig. 6). The interference colors of each grain are defined by their *c*-axis orientation with respect to the crossed-polarized light, the line of sight, and the thickness of the grain (Owen and Hendrikse, 2023), with the exception of the regions near the corners of the glass plates. Unfortunately, the glass plates contained stress-induced birefringence from the manufacturing process, resulting in a superposition of birefringence of the ice sandwiched between the glass plates. Nevertheless, at the beginning of all tests, the ice specimen was loaded rapidly until brittle fracture, which was visually accompanied by a stress-induced birefringence change (Ravi-Chandar et al., 1994) in the ice grains (see Fig. 7). An example of how the stress-induced birefringence change relates to the load patterns during a crushing cycle is given in the next section.

For all tests, fracture was observed at high velocity. Fracture was characterized by cracks at two scales (see Fig. 8), one on the order of the ice specimen size (herein termed macrocrack), and the other on the order of the grain columnar diameter (herein termed microcrack). Microcracks typically emanated from macrocracks, but also occasionally developed randomly within the specimen. The microcracks propagated in clusters around the macrocracks and along grain boundaries. The densification of microcracks with deformation eventually led to either partial or complete opacity of the ice specimen.
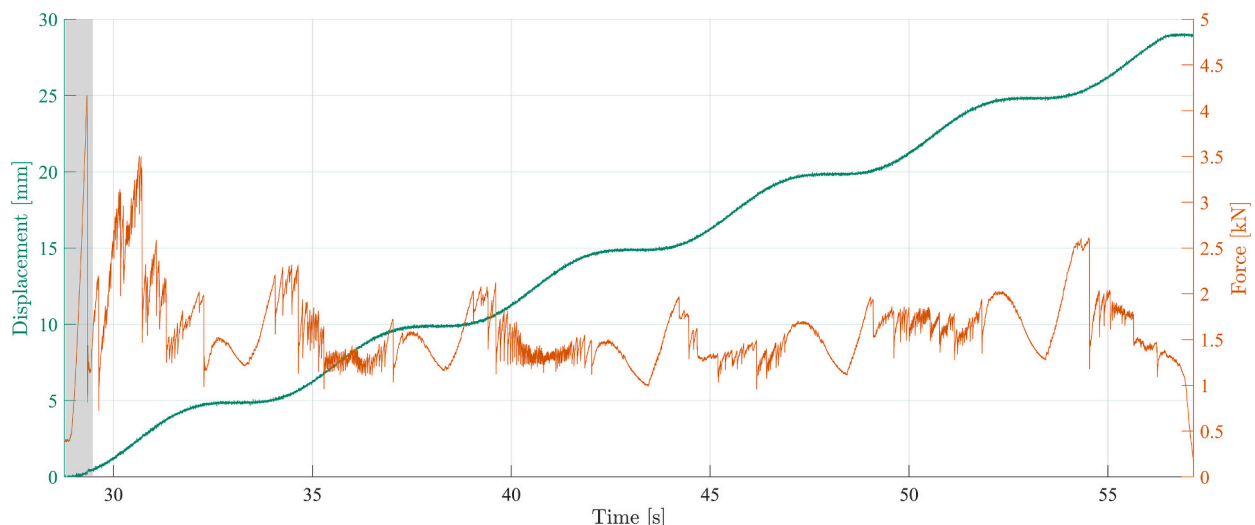

Fig. 4. Time series of indentor plate displacement and load from the results of Test #2. The grey region delineates the initial loading and fracture.
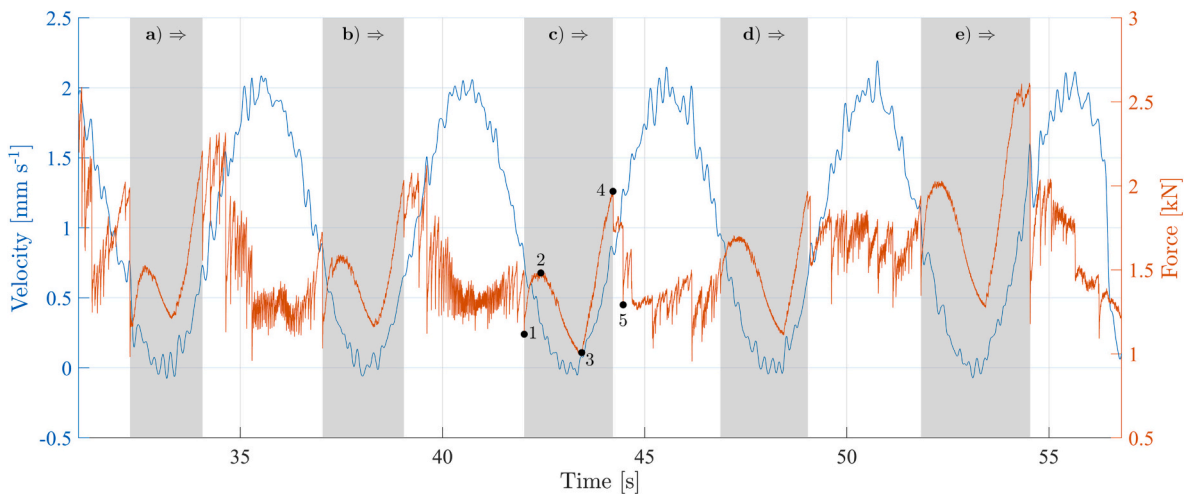
Fig. 5. Time series of indentor plate velocity and load from the results of Test #2. Each grey region a)-e) delineates the period of low velocity and non-brittle ice behavior, with brittle ice behavior subsequently in each cycle as indicated by the arrows.
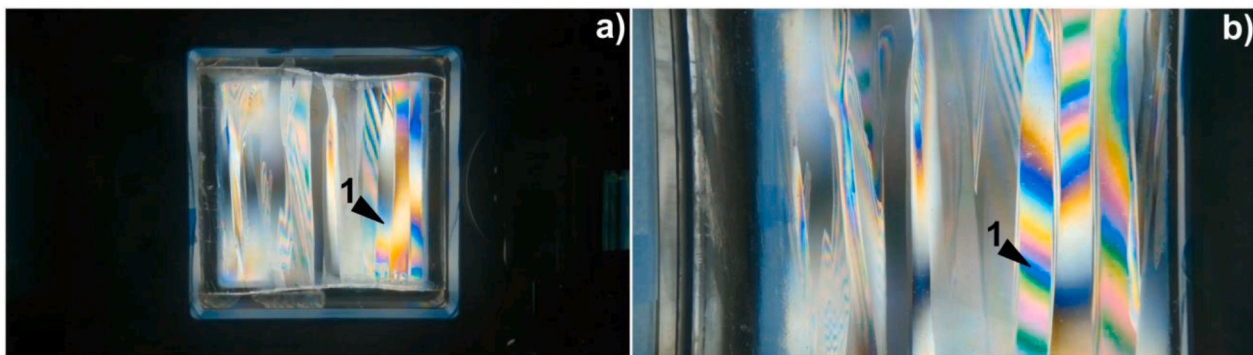

Fig. 6. Frames from the a) global straight, and b) close-up oblique video views of Test #2 prior to loading. Indicator 1 points to the same location in both views. Note the differences in interference colors due to the difference in line of sight relative to the direction of the transmitted crossed-polarized light.

4. Results

The test results are presented in the form of time series, statistics, and video frames to illustrate the behavior of ice deformation and failure behavior and the corresponding load patterns. First, attention is given to one particular test for conciseness to highlight key features of the ice deformation and failure behavior, which can be generalized to all tests with a haversine velocity waveform ($\alpha = 1$). Second, trends are identified from the stress relaxation durations and load peaks of all tests with a haversine velocity waveform. Third, a test with a velocity waveform which deviated from the haversine ($\alpha < 1$) is presented to show the effect on the ice deformation and failure behavior and consequent relaxation duration and peak loads.

4.1. Ice deformation and failure behavior during a crushing cycle

Using Test #2 as an exemplar of the ice behavior during individual velocity oscillations, called crushing cycles, specific features from the velocity and load time histories can be discerned and are delineated by the grey regions in Fig. 4. During high velocity, above about 0.8 mm s^{-1}, brittle crushing dominated the load signal with sawtooth-like load drops. But during the period of low velocity—delineated by each grey region—the fracture was interrupted. The load first increased to a plateau, then decreased with decreasing velocity until the velocity began increasing again. Once velocity began increasing, or i.e. the acceleration became positive, the load immediately began increasing and continued to increase to a high velocity until fracture. The load at

fracture was consequently higher than the load peaks during prior brittle crushing. No significant fracture events or cracking were observed during the period in each grey region, as confirmed by the video and changes between video frames (see Fig. 9). However, stress-induced interference color change was observed in relatively undamaged grains which were loaded and unloaded. It also appeared from the difference between video frames in the right column of Fig. 9 that deformation at grain boundaries from Marker 1 to Marker 4 were also visible. Upon fracture between Marker 4 and Marker 5, the stress-induced birefringence did not appear to markedly change.

Strikingly, the peaks in Fig. 5 immediately following the non-brittle behavior were higher than any other peak thereafter during the portion of the cycle with brittle behavior. This observation was consistent for all of the cycles in Test #2 after the first series of fracture in the beginning of the experiment. This observation suggests that a load-history or memory effect, a rate-dependent hysteresis, contributed to the change in the peak loads following non-brittle behavior.

4.2. Effect of velocity on load peaks during a crushing cycle

To further illustrate this point, Fig. 10 presents the peak load at fracture at the corresponding velocity for each cycle. Peaks are identified per cycle based on the MATLAB function *findpeaks* with a minimum peak prominence of 4% of the maximum load in each cycle. It can be shown that peak load at fracture varies inversely with velocity, where peak loads are higher for lower velocities. Interestingly, for cycles a) and b) in Fig. 10, the relation between force and velocity suggests a process
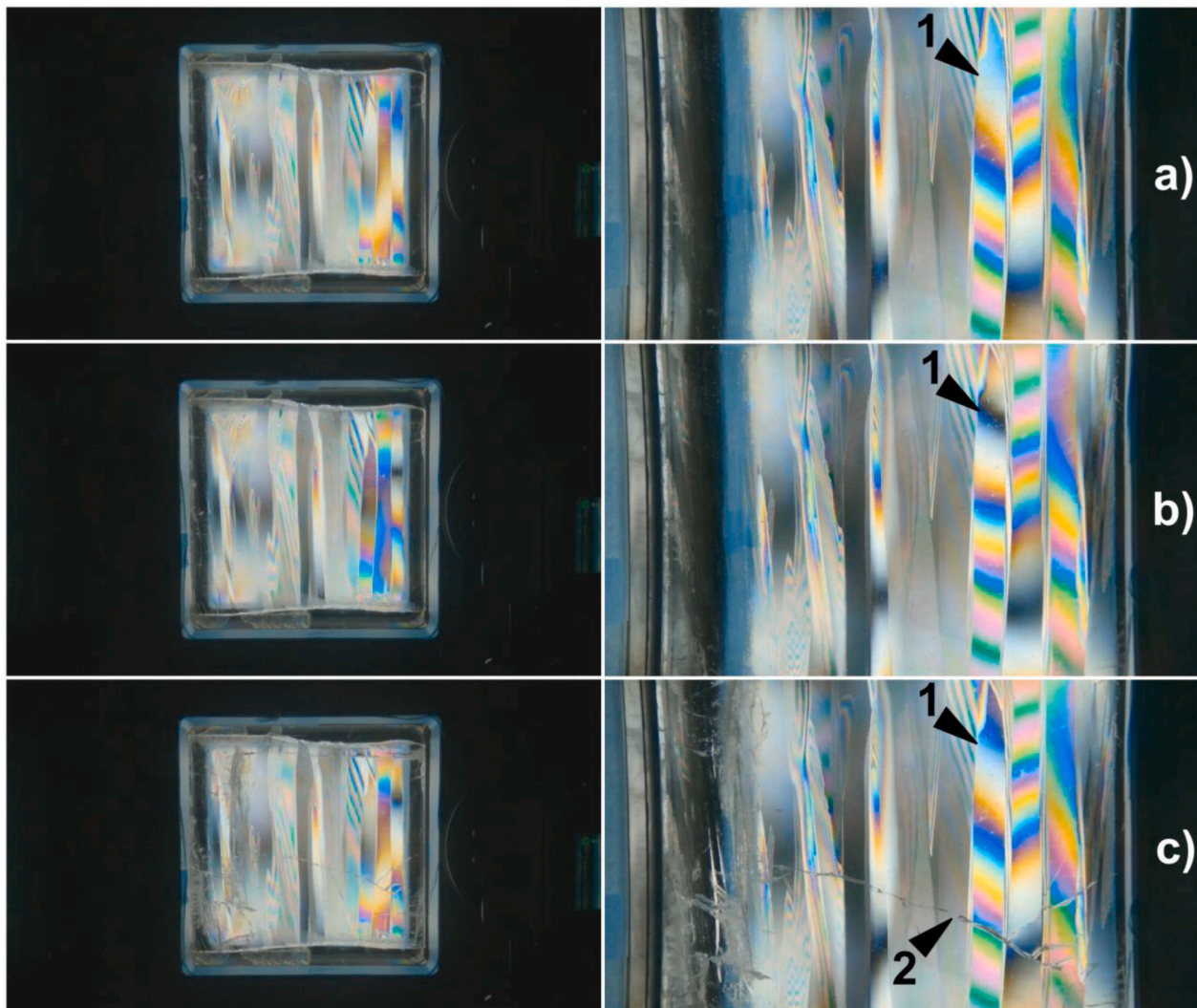
Fig. 7. Global straight and oblique close-up video views from Test #2 with frames a) prior to loading; b) initial loading, just before fracture; and c) immediately after fracture. Indicator 1 points to the same location in each frame, highlighting the change in the shape and color of the interference color pattern in the grain with loading. Indicator 2 points to a large crack which unloaded the grain (compare Indicator 1 in b) and c)).
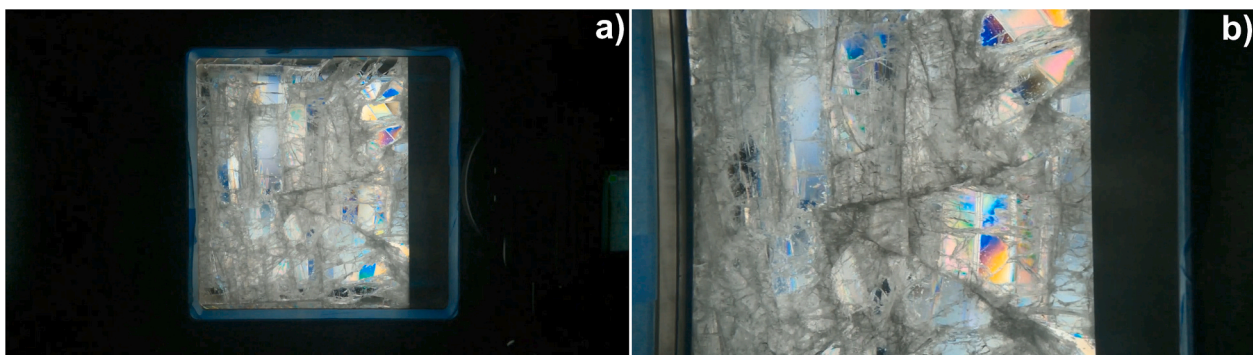

Fig. 8. Frames from the a) global straight, and b) close-up oblique video views of Test #2 at the end of testing (compare with Fig. 5). The ice specimen has become opaque with cracks; however, some portions of grains within the ice specimen remained minimally cracked and clearly retain their interference colors.

which can be described qualitatively by a curve as shown in Fig. 10f. The change in peak load varied not only with velocity but also with the duration during which the velocity was sufficiently low to inhibit fracture. For the peaks immediately following the period of non-brittle behavior, the load was higher and then appeared to reduce with the

number of failure events and with time until the next period of non-brittle behavior (see Fig. 5). It appeared that the load peak-velocity hysteresis that was gained during the period of non-brittle behavior was eventually lost during brittle crushing and was not present in subsequent crushing cycles, i.e. short-term load-history effects on the order of less
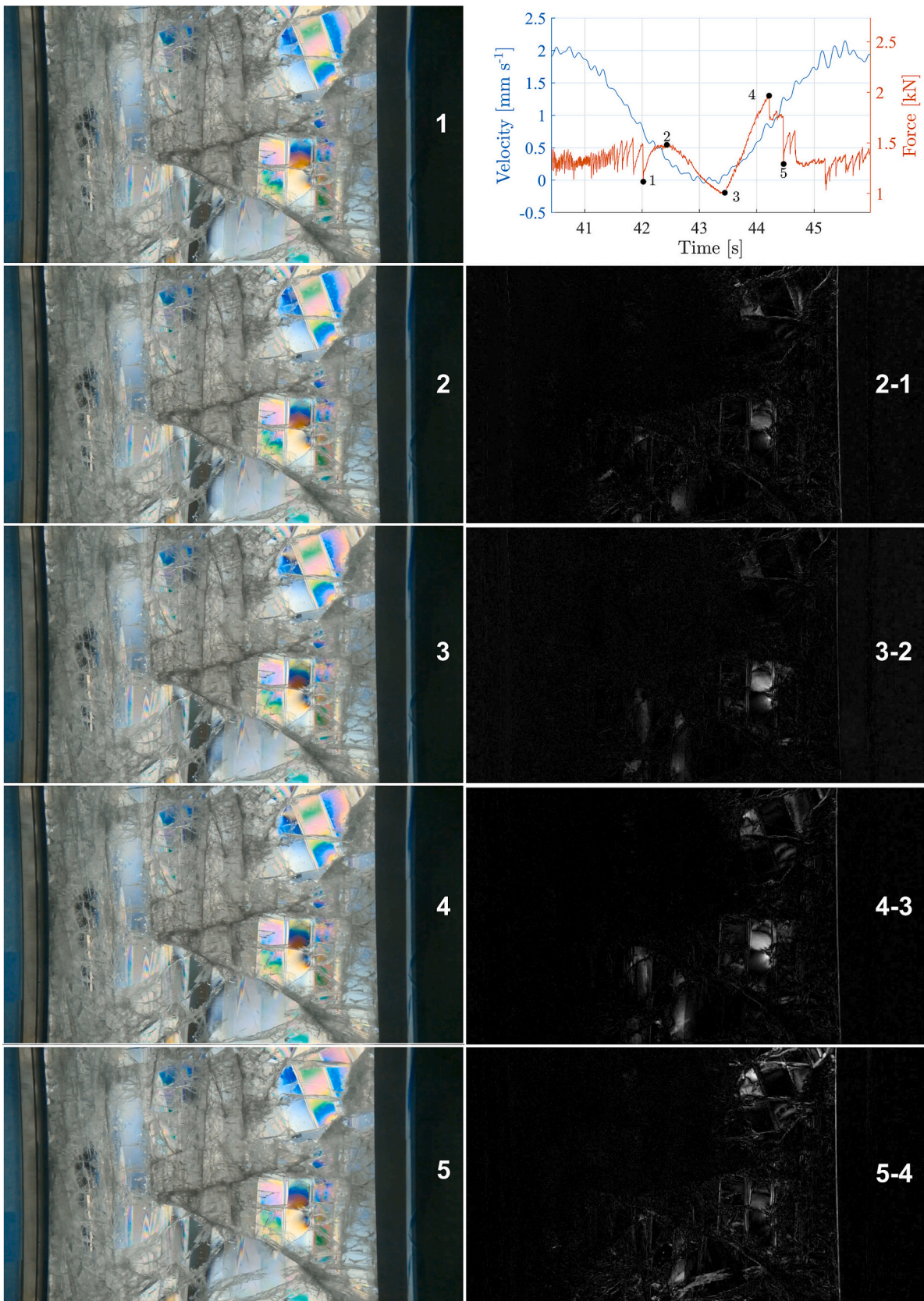
Fig. 9. Left column: video frames (1–5) from Test #2, corresponding to the markers in Fig. 5. Right column: greyscale difference between the video frames (e.g. 2–1 means frame 2 minus frame 1). Top right: reproduced portion of Fig. 5.
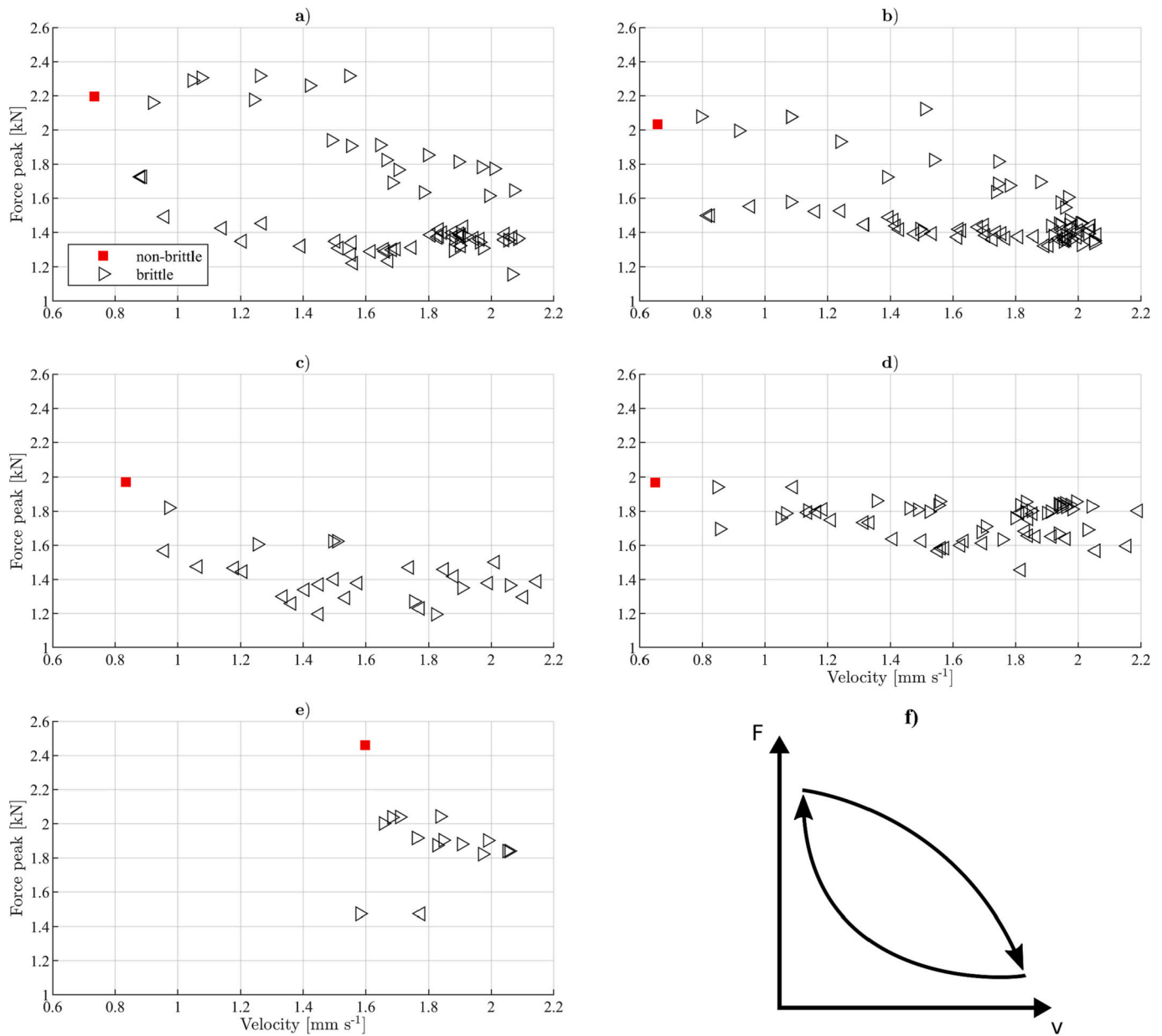
Fig. 10. Force peaks at fracture as a function of velocity for each consecutive crushing cycle a)-e) Fig. 5, Test #2. The force peaks following the period of non-brittle ice behavior are indicated by a red square, and the force peaks during brittle behavior are shown as a triangle. Right-pointing triangles indicate positive acceleration and left-pointing triangles indicate negative acceleration of the indentor plate. f): Observed qualitative relation of rate-dependent hysteresis between peak force at fracture (F) and velocity (v) from cycles a) through d). (For interpretation of the references to color in this figure legend, the reader is referred to the web version of this article.)

than one half of a cycle (< 2.5 s in this case, Test #2). The hysteresis was clearly observed for the first two or three cycles, and was obfuscated with succeeding cycles, which was likely related to the accumulation of damage in the material.

4.3. Effect of velocity on critical deformation between fracture events

Additionally, the deformation between fractures, termed critical (failure) deformation δ_f, was determined by integrating the velocity over the time between load peaks. The critical deformation values from Test #2 are plotted as a function of mean velocity between peaks in Fig. 11. Apart from several outliers, caused by the algorithm missing failure events and thus extending critical deformation, the dichotomy in ice behavior is clear. The critical deformation during non-brittle behavior is higher than during brittle behavior, where the brittle critical

deformation is roughly independent of velocity and can be fitted well with a Weibull probability distribution for Test #2 (see Fig. 11f). The non-brittle critical deformation correlates strongly with a peak load that is mostly, though not always, higher than peak loads during brittle behavior. Comparing the ratio non-brittle to mean brittle critical deformations per cycle and averaging over the five cycles results in a factor of about 6. The results suggest that there was a change in the critical deformation between brittle and non-brittle behavior, allowing for more deformation, and thus more load, to be introduced into the ice prior to fracture.

Extending this analysis to the other tests, the effect of frequency and velocity on stress relaxation duration and peak load are investigated next.
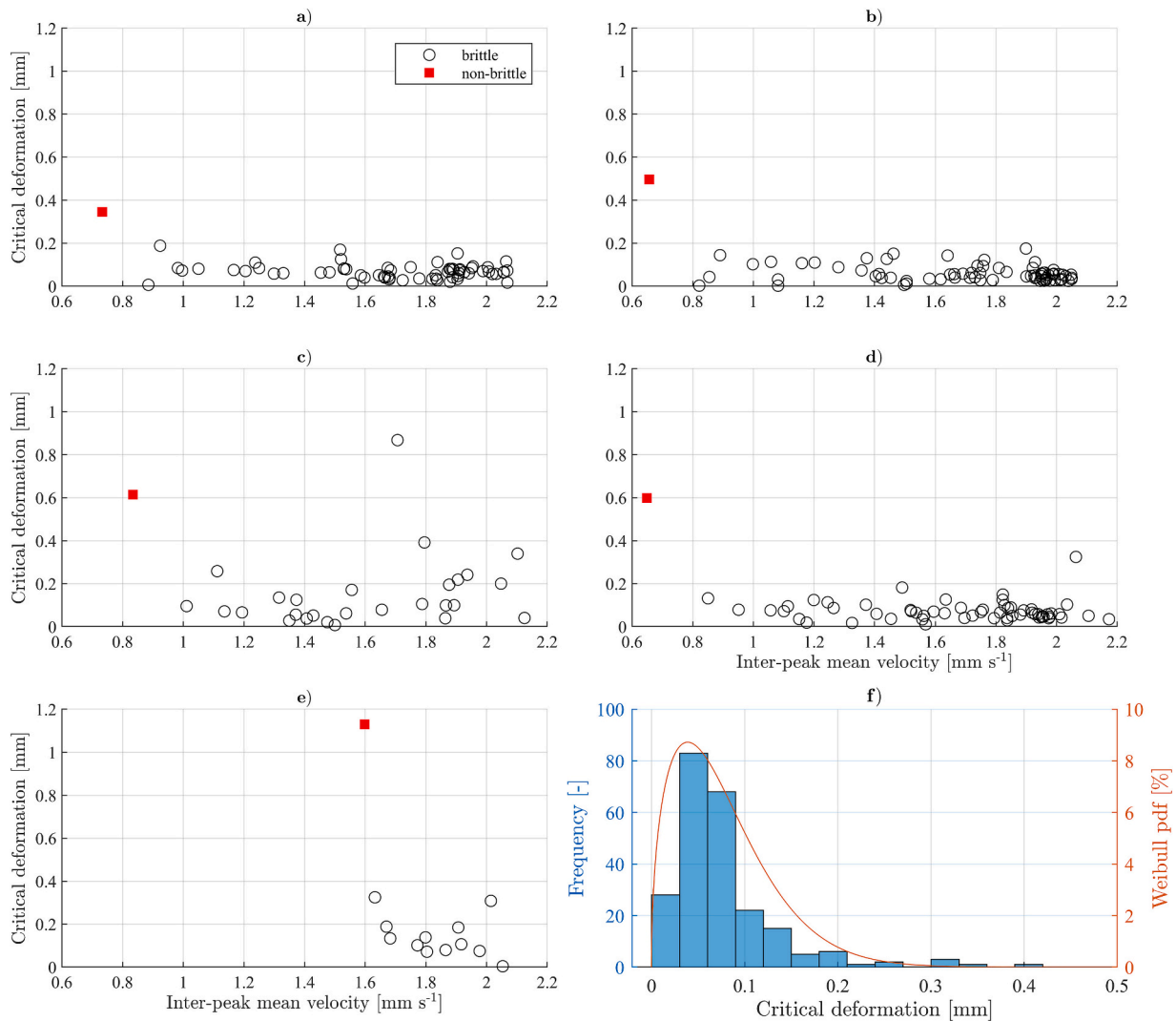
Fig. 11. a)-e) Critical deformation between force peaks against the mean velocity between force peaks from Fig. 5, Test #2. The critical deformation during period of non-brittle ice behavior is indicated by a red square, and the critical deformation during brittle behavior is shown as a circle. f) Distribution of all brittle critical deformation events (black circles) for Test #2, fitted with a Weibull probability distribution function (λ=0.0849, k=1.4615, $\overline{\delta}_{f,brittle}$≈0.08 mm). Note that critical deformation >0.8 mm were treated as outliers and omitted from the fitting.

4.4. Effect of frequency and velocity on stress relaxation duration and peak load

As mentioned previously, for tests where $\alpha = 1$, when the velocity was relatively low and decreasing the brittle failure was interrupted (confirmed by video inspection) and unloading of the ice specimen was observed, where the load signal became smooth. This smooth unloading was associated with a stress relaxation mechanism in the ice which prevented observable fracture and was a function of time at low velocity. Therefore, there was a frequency and velocity dependency of the relaxation, namely in the duration at low velocity. This stress relaxation duration—defined as the duration from the lowest point in the trough of the load signal during non-brittle behavior to the previous peak during non-brittle behavior (e.g. Marker 2 to 3 in Fig. 5)—was determined for all tests. Additionally, all load peaks following the stress relaxations per cycle were identified and the previous brittle peak load was subtracted from each non-brittle load peak, denoted as ΔF. The mean of the ΔF for each test was plotted against the mean stress relaxation duration for each test in Fig. 12. It can be seen that ΔF increases for increasing stress relaxation duration, which is a function of lower frequencies and velocities; i.e. longer durations at low velocity result in higher peak loads.

Negligible peak enhancement was observed for the highest frequency and velocity tested of 2 Hz and 10 mm s^{-1}, respectively.

While stress relaxation duration increased with a decrease in frequency and velocity, it was not apparent whether the duration at low velocity or low velocity itself was contributing to ΔF. Thus, the minimum velocity was increased in some tests by altering the haversine waveform as discussed next.

4.5. Effect of deviation from haversine velocity waveform on load signal

To assess the importance of the duration at low velocity or solely low velocity, several tests were performed in which the velocity waveform deviated from the haversine ($\alpha < 1$, see Eq. 1 and Fig. 3). In effect, this means the minimum velocity was nonzero. For these tests, it was observed that when the velocity was relatively low and decreasing the brittle failure was interrupted but unloading did not necessarily occur (see Fig. 13). Instead, the load remained nearly constant or began increasing with a smooth signal until a fracture event occurred. Therefore, the stress relaxation duration decreased or vanished with a decrease in α for a given velocity and frequency. For example, when comparing Test #10 ($\alpha = 0.5$, Fig. 13) to Test #2 ($\alpha = 1$, see Fig. 5), the
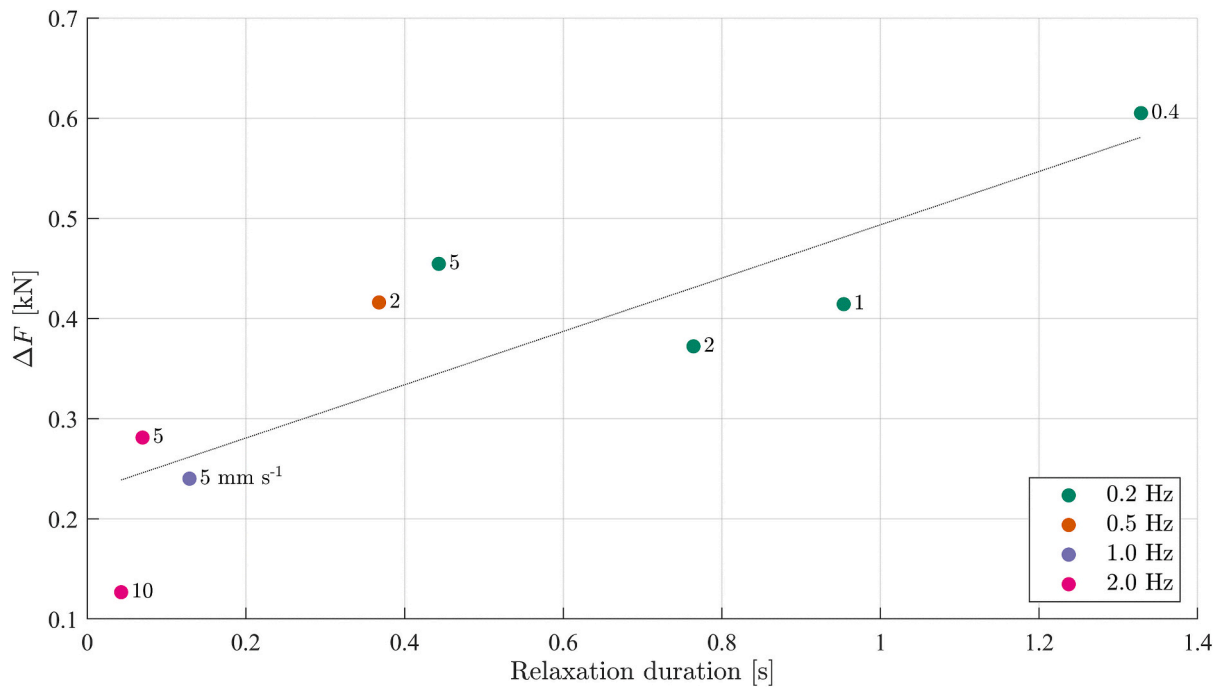
Fig. 12. Difference between non-brittle load peak and previous brittle peak *ΔF* plotted against stress relaxation duration for different velocities and frequencies. Velocities are denoted by numbers next to the points, and frequencies are indicated by colors as shown in the legend. A linear trend is fitted through all data.
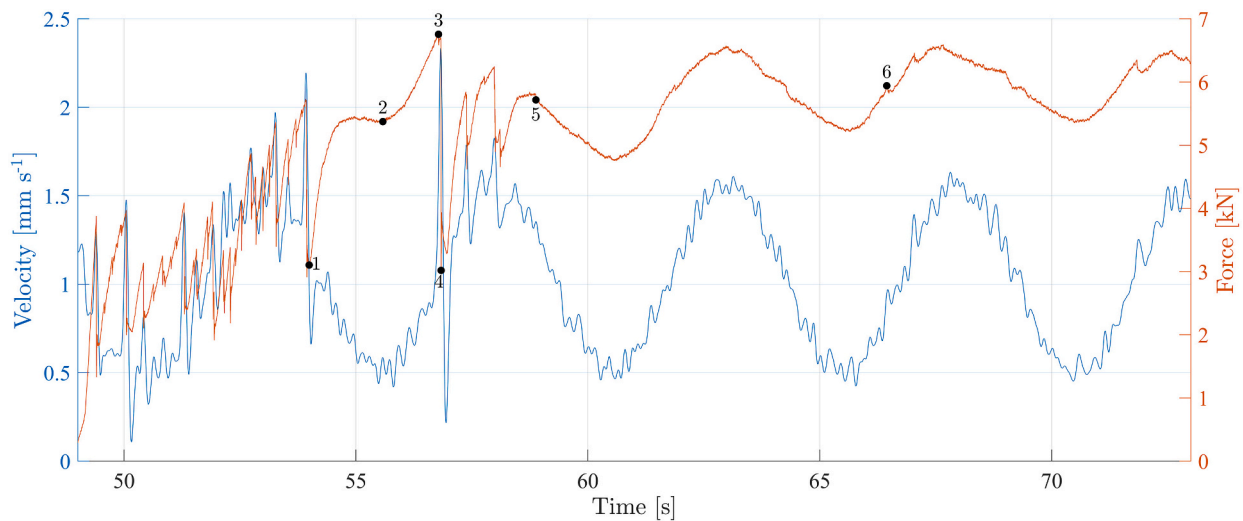

Fig. 13. Time series of indentor plate velocity and load from the results of Test #10. The Markers 1–4 correspond to the video frames in Fig. 14, and the Markers 5–6 correspond to the video frames in Fig. 15.

development of the load during non-brittle behavior with a higher minimum velocity displayed effectively no unloading. Instead, the load plateaued near Marker 2 in Fig. 13 and then increased with increasing velocity. For this particular crushing cycle, due to the high minimum velocity, some microcracks were observed forming near grain boundaries, but their appearance did not result in any change in the behavior of the load pattern during non-brittle behavior (see Fig. 14). Interestingly, from Marker 1 to Marker 3, stress-induced change in interference colors and/or deformation at grain boundaries showed clearly in the difference between video frames. This clarity was lost once the large fracture at Marker 4 appeared to dissipate the deformation at the grain boundaries.

Curiously, after Marker 5 in Fig. 13, the load behavior exhibited a smooth pattern following the velocity of the indentor plate, with no

significant fracturing visible in the load signal. Upon inspection of the videos, it was observed that such significant damage accumulated in the ice specimen that the deformation behavior no longer showed globally brittle failure (see Fig. 15).

It should be noted that the loads for Test #10 were higher in general than those from Test #2, but the reason for the disparity could not be clearly identified. Nevertheless, it was found that the critical deformation between Marker 1 and 3 was 2.0 mm and failure occurred at 1.6 mm s^{-1}. Comparing Test #10 to Test #2, preliminary results showed that the critical deformation was greater and fracture occurred at a higher velocity in the case that the minimum velocity did not reach zero and unloading was inhibited. However, more tests are required to further address these observations and determine reliable trends.
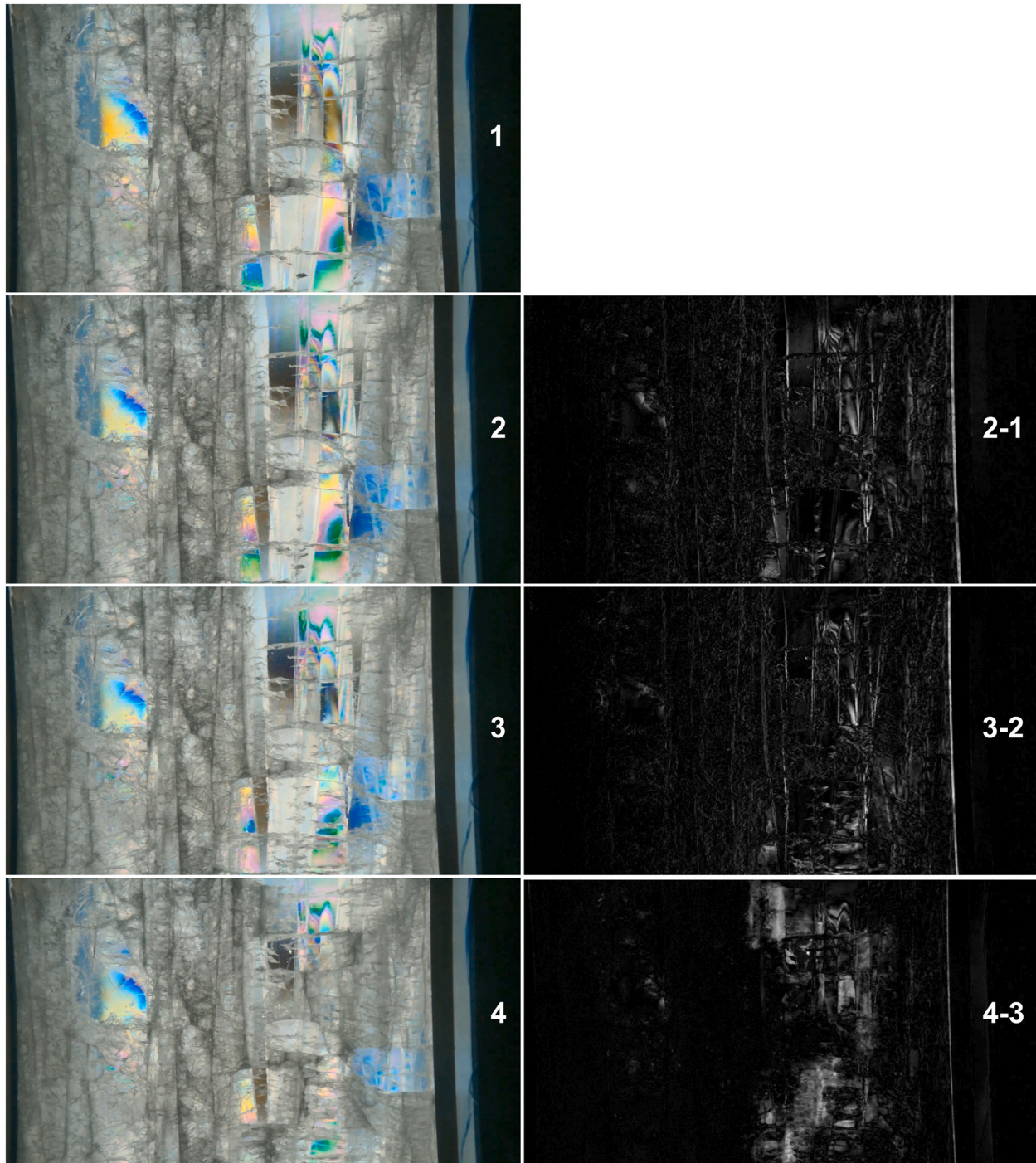
Fig. 14. Left column: video frames (1–4) from Test #10, corresponding to the markers in Fig. 13. Right column: greyscale difference between the video frames (e.g. 2–1 means frame 2 minus frame 1).

5. Discussion

The results shown in the present study demonstrated a dichotomy in confined, freshwater columnar ice specimen deformation behavior as a function of imposed velocity and frequency: brittle at high velocity and non-brittle at low velocity. The sawtooth-like load pattern at high velocity appeared very similar to the results from other freshwater ice crushing experiments under similar conditions (Gagnon and Bugden, 2008; Tuhkuri, 1995). As for the non-brittle behavior at low velocity, small-scale ice penetration experiments with sufficiently compliant structures (Sodhi, 1991; van den Berg et al., 2022; Yap, 2011) and

controlled-oscillation experiments (Hendrikse and Metrikine, 2016) showed similar load patterns. However, according to the knowledge of the authors, no other ice crushing experiments have been performed that varied the deformation rate by many orders of magnitude during a single test. Constant-rate crushing experiments, even at low velocities or strain rates, may not expose the change in ice behavior, especially the load peak-velocity hysteresis, that has been demonstrated in the present study. It should be emphasized again that the test setup was not completely rigid, which had implications for the results obtained in the present study, as discussed next.
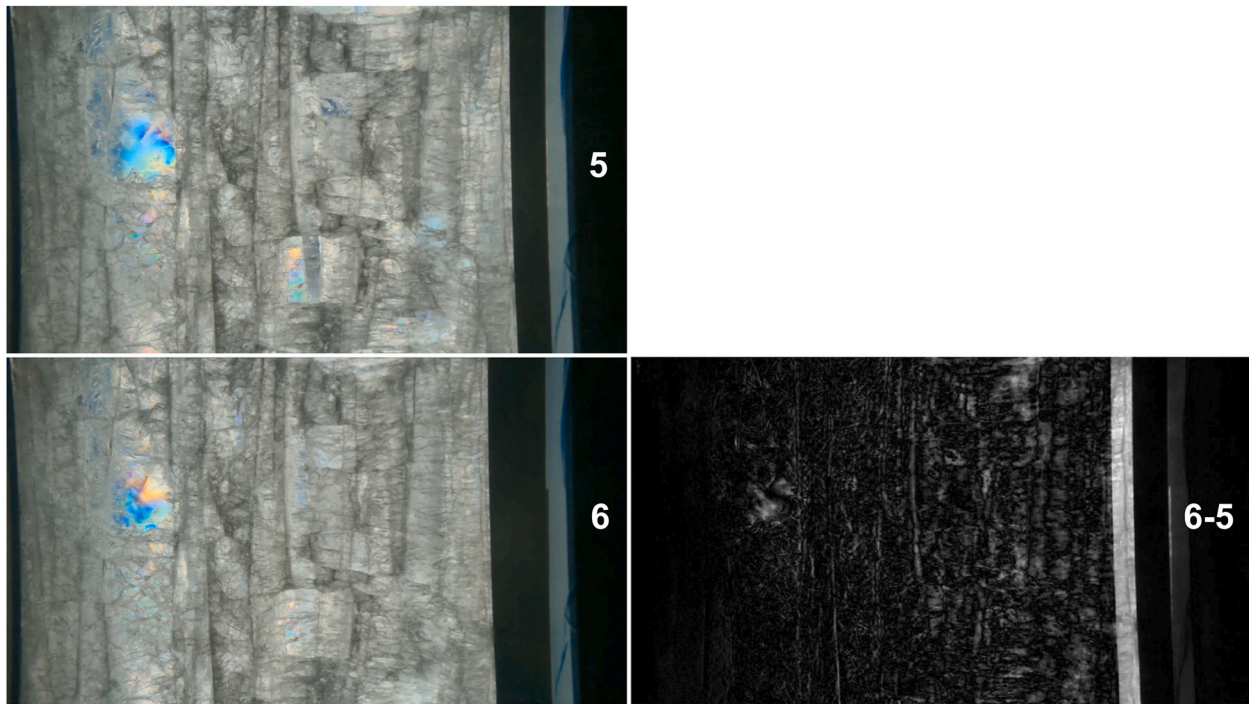
Fig. 15. Left column: video frames (5–6) from Test #10, corresponding to the markers in Fig. 13. Right column: greyscale difference between the video frames (e.g. 6–5 means frame 6 minus frame 5).

5.1. Effect of lack of test setup stiffness on results

Although the test setup was relatively rigid, this rigidity was not maintained when significant load drops occurred as previously mentioned. The major consequence of this lack of stiffness was observed in the velocity signals, which were derived from the displacement measurements. Small transient vibrations in the displacement measurements after large load drops resulted in large velocity fluctuations.

These velocity fluctuations were not experienced by the ice specimen as confirmed by the absence of fluctuations in the load signals, and significant low-pass filtering was needed to clearly identify the velocity of the indentor plate after large load drops. The critical deformation values, which were calculated from the filtered velocity signals, were sensitive to the transient vibrations and the type and magnitude of filtering. The transient vibrations were superimposed on the indentor plate velocity, which occasionally led to over- or underestimations of the
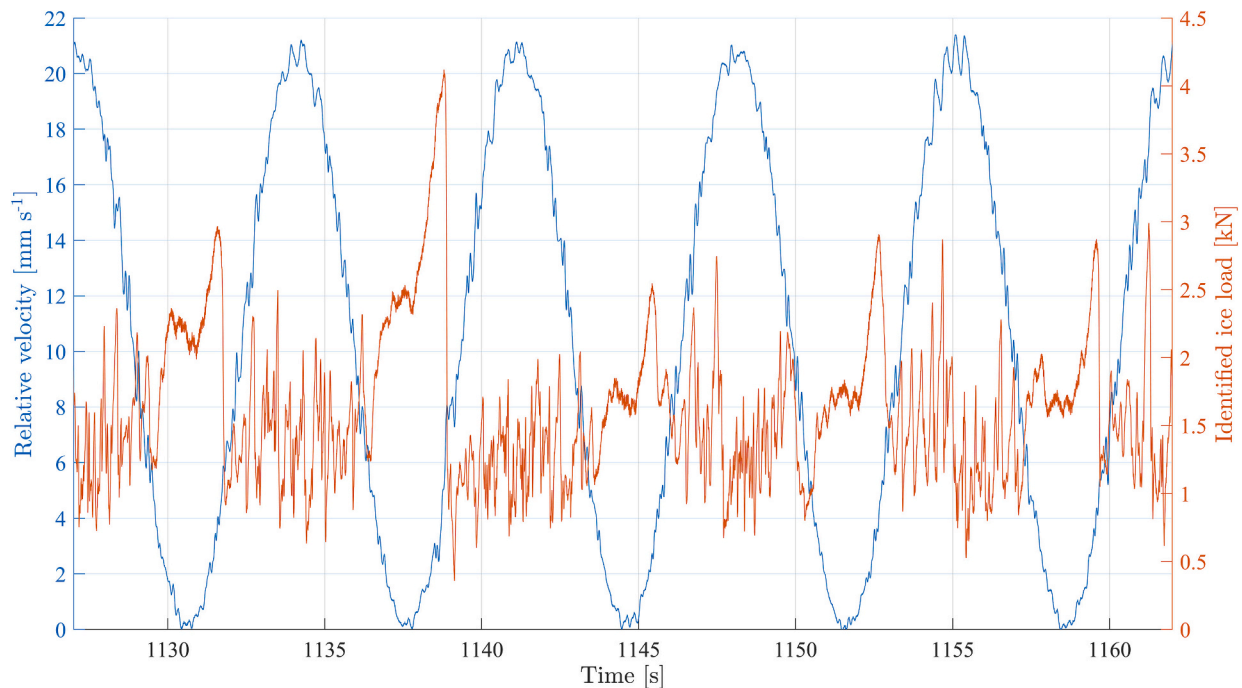

Fig. 16. Sample time series of relative velocity and identified ice load from controlled oscillation ice tank test ID 428 (Hendrikse et al., 2022). The controlled oscillation frequency was 0.154 Hz, the amplitude of oscillation was 11 mm, and the carriage velocity was 10 mm s^{-1}.

critical deformation between peaks (e.g. see Fig. 11c). Given the uncertainty caused by the test setup flexibility in the velocity signals, quantitative observations from a single test were provided about the critical deformations but were not compared across tests. While the test setup was relatively compliant due to large load drops, the results showed the ice behavior to be consistent across a range of speeds and frequencies. Next, the results from the present study are compared with model-scale controlled-oscillation ice tank tests to demonstrate consistency of ice behavior for a different ice type and loading scenario.

5.2. Comparison to controlled-oscillation in model-scale ice tank tests

Model-scale ice tank tests with controlled oscillation of a rigid, vertically sided aluminum pile penetrated through floating ethanol ice at an air temperature of −11 °C were performed at various ice drift speeds, frequencies, and amplitudes of oscillation (Hendrikse et al., 2022). Fig. 16 presents a sample time series of test ID 428 in which the frequency of oscillation was 0.154 Hz, the amplitude of oscillation was 11 mm, and the ice drift speed was 10 mm s^{-1}. It can be clearly seen that brittle behavior of the ice occurred at high velocity and high load peaks developed during periods of low relative velocity. Additionally, some minor stress relaxation can be seen to occur in a few cycles prior to the high load peak and global ice failure. No evidence of hysteresis can be discerned from the load signal, in comparison to the results of the present study. Nonetheless, the load pattern is surprisingly similar between the present study and the controlled oscillation in the model ice and wave tank. It should be emphasized that the model ethanol ice was rather different in microstructure and temperature profile, yet yielded such qualitatively similar load patterns, albeit at an order of magnitude higher velocity than the results from larger-grained freshwater ice.

5.3. Reflection on literature and anelasticity of ice

While the observations of brittle ice behavior at high velocity and non-brittle at low velocity align with the ductile-to-brittle transitional behavior phenomenon, this phenomenon was founded on uniaxial compression and indentation tests, each at a constant stress or strain rate of sufficient duration to expose steady-state deformation or failure behavior (Michel and Toussaint, 1977). Additionally, the experiments were generally performed on undamaged specimens and subjected to monotonic stress-controlled deformation, as opposed to the crushing cycles of the present study as a result of the haversine velocity waveform, i.e. strain-rate-varying strain-controlled deformation. Strain-controlled cyclic compression of ice was performed by Heijkoop et al. (2018), but without significant final strain or failure of the specimens. Additionally, numerous studies on uniaxial and confined, stress-controlled cyclic compression have been performed (Cole et al., 1998; Cole and Durell, 1995; Iliescu and Schulson, 2002; Wei et al., 2022, 2020). However, such tests cannot be performed beyond catastrophic failure of the specimen as the stress cannot be controlled upon failure. Moreover, strain-controlled, not stress-controlled, experiments better represent the loading scenario associated with frequency lock-in vibrations. In summary, previous experiments focused on constitutive modeling of ice have not adequately captured the strain-controlled continuous crushing and cyclic failure needed for investigating the ice mechanics in frequency lock-in, and are thus unable to be directly compared to the present study.

Regarding the failure modes of the confined ice specimens in the present study, splitting in the direction of loading was suppressed and faulting became more prevalent with the added confinement of the acrylic plates, as similarly found in literature (Wachter et al., 2009). Compression experiments with cylindrical freshwater ice specimens displayed various failure modes depending on the temperature, stress state, and strain rate scenarios. For triaxial conditions, ductile-type flow developed for higher temperatures, higher confinement pressures, and lower strain rates, and shear fracturing or faulting occurred for lower

temperatures, higher confinement pressures and higher strain rates. Axial splitting occurred for lower temperatures, the lowest confinement pressures, and higher strain rates (Barrette and Jordaan, 2001; Meglis et al., 1999; Rist and Murrell, 1994; Stone et al., 1997). For uniaxial conditions, axial splitting dominated as the main failure mode at higher strain rates when end zones of the specimen were constrained, and shear faulting otherwise, and ductile-type flow developed at lower strain rates (Hawkes and Mellor, 1972; Jordaan et al., 1992; Mellor and Cole, 1983; Schulson, 1990; Schulson et al., 1989).

Based on the videos, no evidence of dynamic recrystallization in the ice specimen was observed. Whether dynamic recrystallization played a role in high-pressure zones at the ice-indentor interface could not be discerned from the results as contact area, confinement, and detailed high-speed video were not available for measurements. However, it was unlikely that sufficient pressures and confinement were present to cause recrystallization as observed in triaxial compression studies (Barrette and Jordaan, 2003; Jordaan, 2001; Meglis et al., 1999; Melanson et al., 1999).

The mechanism of creep or viscous straining generally refers to deformation at time scales on the order of 10^3 s (Cole, 2001), which would not be relevant for the tests performed in the present study. The prospect of accelerated or enhanced creep in the tertiary regime from microcracking at high homologous temperatures (Jordaan et al., 1992; Sinha, 1989) might aid in explaining whether creep in the ductile-to-brittle transition can participate at time scales relevant for frequency lock-in vibrations of structures with natural periods on the order of 1 s.

Due to stresses and the significant damage in the ice during the experiments, and especially at high homologous temperature ($T_H = 0.97T_{mp}$ in the present study, where T_{mp} is the melting point of freshwater ice), cohesion and the possibility of rapid crack healing via sintering may be involved (Murdza et al., 2022; Szabo and Schneebeli, 2007). However, it was not possible to accurately measure temperature changes throughout the specimens in the present study.

In the present study, a hysteresis was observed in the load behavior, which appeared to develop in the ice as a result of the duration at low velocity, followed by rapidly increasing the velocity. This load peak-velocity hysteresis, and the dichotomy in ice behavior, might be explainable using a framework of dislocation-based mechanics (Cole, 2021; Schulson et al., 2019). The load-history effect, and possible strengthening, may relate to back stresses as observed in cyclic flexure of ice beams (Murdza et al., 2021, 2020) and developing as a result of high stress and stress rate during the unloading and reloading in the non-brittle period. Evidence for higher stresses upon reloading in a roughly similar manner as in the present study have been observed in a yield phenomenon in cold single crystals of metals (Haasen and Kelly, 1957) and in dynamic strain aging of polycrystalline metals (Ren et al., 2017).

The dichotomy in ice behavior might be explained by anelastic ice properties of dislocation and/or grain boundary relaxations competing rapidly (< 2.5 s) in time at crack tips to delay fracture when sufficient time and stress are present to produce and mobilize dislocations and/or cause grain boundary sliding (Cole, 2020, 1995). Although this mechanism is described by Schulson and Duval (2009) as the competition between creep and fracture in the ductile-to-brittle transition, the term creep connotes large time scales which are not applicable in this context. Thus, it is clarified here that anelasticity, not creep, manifests in the competition with fracture.

5.4. Application to the frequency lock-in regime

The crushing regime of ice-induced vibrations called frequency lock-in, at least for a single-degree-of-freedom oscillator, is characterized by a near-sinusoidal structural response. In frequency lock-in, during the period of low relative velocity between ice drift and structure, the global ice load typically shows a peak greater that those during high relative velocity. Moreover, the brittle load pattern at high relative velocity is mostly absent from the period of low relative velocity (van den Berg

et al., 2022). It is speculated that the results from the present study and the observations of frequency lock-in vibrations from small-scale experiments may be governed by the same mechanism: dislocation mechanics. The dislocation mechanics are involved in anelasticity and back stress, which are responsible for the change in ice behavior during the period of low relative velocity between ice and structure and the subsequent high peak load. The global load during low relative velocity can transfer more energy to the structure in that part of the cycle than can be extracted during brittle crushing in the rest of the cycle. This mechanism can sustain frequency lock-in vibrations, but is self-limiting in terms of the structural velocity. When more energy is transferred to the structure than is needed to sustain the near-harmonic response, the structural velocity greatly exceeds the ice drift speed, which causes unloading of the structure as the structure loses contact with the intact ice sheet. As long as the structural velocity does not greatly exceed the ice drift speed, the ice conditions remain stable, and the duration of low relative velocity is sufficiently long to delay fracture and cause a following high load peak, sustained vibrations can develop. While this description follows the established frequency lock-in velocity relation (Toyama et al., 1983), it again implicitly suggests the inclusion of a duration component which depends on the natural frequency of the structure (Hendrikse and Metrikine, 2016). Finally, the hysteresis of the load increase after a duration of low relative velocity could be considered in research on ice-induced vibrations of vertically sided structures, a critical observation which should be further studied.

The new results in the present study are significant because they demonstrate that the ice-induced vibrations problem, and specifically frequency lock-in, requires ice to be treated as a loading-history, and thus time-dependent, material at short time scales, which contradicts the assumptions of some numerical ice models (Gagnon, 2022; Matlock et al., 1969) and dimensional analyses (Korzhavin, 1962; Palmer et al., 2010). The implications in practice for these results are that such numerical ice models and dimensional analyses may yield inaccurate predictions of the development of ice-induced vibrations, and only models which consider ice as a loading-history-dependent material at short time scales may be able to grant accurate predictions (Hendrikse et al., 2018; Huang and Liu, 2009; Kärnä et al., 1999).

The present study and the research on anelasticity would suggest that some of the processes involved in the development of ice-induced vibrations occur at scales smaller than the grain. This finding is encouraging for further research in dislocation mechanics during cyclic compressive loading of ice. The scaling of loads and motions in ice-induced vibrations could benefit from the findings with further investigation of viscosity in ice and dislocation-based mechanics.

6. Conclusion

The results presented in this study demonstrated a dichotomy in confined, freshwater columnar ice specimen deformation behavior as a function of imposed velocity and frequency: brittle at high velocity and non-brittle at low velocity. At low velocity, ice fracture is interrupted and stress relaxation occurred until the velocity began increasing in the cycle. The stress relaxation in the load is accompanied by stress-optic effects in the ice. It is found that a load peak-velocity hysteresis developed in each crushing cycle: peak loads following the non-brittle behavior are temporarily higher than the peak loads of the brittle behavior. The temporary load peak enhancement tended to increase with increasing duration of stress relaxation, i.e. the peak enhancement tended to increase with decreasing velocity and frequency. Negligible peak enhancement and stress relaxation duration were observed for the highest frequency and mean velocity tested of 2 Hz and 10 mm s^{-1}, respectively. For tests with a minimum velocity of 1 mm s^{-1}, no stress relaxation was observed in the load measurement. Preliminary results from deviating from the haversine velocity waveform by increasing the minimum velocity showed that the stress relaxation duration decreases, but the non-brittle peak load does not decrease. It is speculated that ice

anelastic ice behavior could account for the rapid stress relaxation at low velocity. It is unclear what causes the hysteresis, although it is speculated that dynamic strain aging might play a role. The change in ice behavior during the experiments demonstrates a mechanism which develops rapidly and might therefore incite the development of the frequency lock-in regime of ice-induced vibrations of vertically sided structures.

CRediT authorship contribution statement

Cody C. Owen: Conceptualization, Methodology, Software, Validation, Formal analysis, Investigation, Resources, Data curation, Writing – original draft, Visualization, Project administration. **Tim C. Hammer:** Software, Investigation, Writing – review & editing. **Hayo Hendrikse:** Conceptualization, Resources, Writing – review & editing, Funding acquisition, Supervision.

Declaration of Competing Interest

The authors declare that they have no known competing financial interests or personal relationships that could have appeared to influence the work reported in this paper.

Data availability

The data are available here: https://doi.org/10.4121/22047680.v1

Appendix A. Supplementary data

Supplementary data to this article can be found online at https://doi.org/10.1016/j.coldregions.2023.103816.

References

Barrette, P., Michel, B., Stander, E., 1993. On the reproduction of ice from a common seed. J. Cryst. Growth 131, 153–156. https://doi.org/10.1016/0022-0248(93)90408-O.

Barrette, P.D., Jordaan, I.J., 2001. Creep of ice and microstructural changes under confining pressure. In: Murakami, S., Ohno, N. (Eds.), Proceedings of the IUTAM Symposium on Creep in Structures. Kluwer Academic Publishers, Springer, Nagoya, Japan, pp. 479–488. https://doi.org/10.1007/978-94-015-9628-2_46.

Barrette, P.D., Jordaan, I.J., 2003. Pressure-temperature effects on the compressive behavior of laboratory-grown and iceberg ice. Cold Reg. Sci. Technol. 36, 25–36. https://doi.org/10.1016/S0165-232X(02)00077-0.

van den Berg, M., Owen, C.C., Hendrikse, H., 2022. Experimental study on ice-structure interaction phenomena of vertically sided structures. Cold Reg. Sci. Technol. 201, 103628 https://doi.org/10.1016/j.coldregions.2022.103628.

Björk, B., 1981. Ice-Induced Vibration of Fixed Offshore Structures, Part 2: Experience with Baltic Lighthouses.

Cole, D.M., 1995. A model for the anelastic straining of saline ice subjected to cyclic loading. Philos. Mag. A 72, 231–248. https://doi.org/10.1080/01418619508239592.

Cole, D.M., 2001. The microstructure of ice and its influence on mechanical properties. Eng. Fract. Mech. 68, 1797–1822. https://doi.org/10.1016/S0013-7944(01)00031-5.

Cole, D.M., 2020. On the physical basis for the creep of ice: the high temperature regime. J. Glaciol. 66, 401–414. https://doi.org/10.1017/jog.2020.15.

Cole, D.M., 2021. A Constitutive Model for Sea Ice: Physical Basis, Formulations, Examples and Applications, in: Proceedings of the 26th International Conference on Port and Ocean Engineering under Arctic Conditions. POAC, Moscow, Russia, pp. 1–12.

Cole, D.M., Durell, G.D., 1995. The cyclic loading of saline ice. Philos. Mag. A 72, 209–229. https://doi.org/10.1080/01418619508239591.

Cole, D.M., Johnson, R.A., Durell, G.D., 1998. Cyclic loading and creep response of aligned first-year sea ice. J. Geophys. Res. Ocean. 103, 21751–21758. https://doi.org/10.1029/98JC01265.

Gagnon, R., 2022. Spallation-based numerical simulations of ice-induced vibration of structures. Cold Reg. Sci. Technol. 194, 103465 https://doi.org/10.1016/j.coldregions.2021.103465.

Gagnon, R.E., Bugden, A., 2008. 2-Dimensional Edge Crushing Tests on Thick Sections of Ice Confined at the Section Face, in: Proceedings of the 19th IAHR International Symposium on Ice. IAHR, Vancouver, British Columbia, Canada, pp. 973–991.

Haasen, P., Kelly, A., 1957. A yield phenomenon in face-centered cubic single crystals. Acta Metall. 5, 192–199. https://doi.org/10.1016/0001-6160(57)90165-7.

Hammer, T.C., van Beek, K., Koning, J., Hendrikse, H., 2021. A 2D Test Setup for Scaled Real-Time Hybrid Tests of Dynamic Ice- Structure Interaction, in: Proceedings of the 26th International Conference on Port and Ocean Engineering under Arctic Conditions. POAC, Moscow, Russia, pp. 1–13.

Hammer, T.C., Willems, T., Hendrikse, H., 2023. Dynamic ice loads for offshore wind support structure design. Mar. Struct. 87, 103335 https://doi.org/10.1016/j.marstruc.2022.103335.

Hawkes, I., Mellor, M., 1972. Deformation and fracture of ice under uniaxial stress. J. Glaciol. 11, 103–131. https://doi.org/10.3189/S002214300002253X.

Heijkoop, A.-N., Nord, T.S., Høyland, K.V., 2018. Strain-Controlled Cyclic Compression of Sea Ice, in: Proceedings of the 24th IAHR International Symposium on Ice. IAHR, Vladivostok, Russia, pp. 118–127.

Hendrikse, H., Metrikine, A., 2015. Interpretation and prediction of ice induced vibrations based on contact area variation. Int. J. Solids Struct. 75–76, 336–348. https://doi.org/10.1016/j.ijsolstr.2015.08.023.

Hendrikse, H., Metrikine, A., 2016. Edge indentation of ice with a displacement-controlled oscillating cylindrical structure. Cold Reg. Sci. Technol. 121, 100–107. https://doi.org/10.1016/j.coldregions.2015.10.013.

Hendrikse, H., Nord, T.S., 2019. Dynamic response of an offshore structure interacting with an ice floe failing in crushing. Mar. Struct. 65, 271–290. https://doi.org/10.1016/j.marstruc.2019.01.012.

Hendrikse, H., Ziemer, G., Owen, C.C., 2018. Experimental validation of a model for prediction of dynamic ice-structure interaction. Cold Reg. Sci. Technol. 151, 345–358. https://doi.org/10.1016/j.coldregions.2018.04.003.

Hendrikse, H., Hammer, T.C., van den Berg, M., Willems, T., Owen, C.C., van Beek, K., Ebben, N.J.J., Puolakka, O., Polojärvi, A., 2022. Experimental data from ice basin tests with vertically sided cylindrical structures. Data Br. 41, 107877 https://doi.org/10.1016/j.dib.2022.107877.

Huang, G., Liu, P., 2009. A dynamic model for ice-induced vibration of structures. J. Offshore Mech. Arct. Eng. 131, 1–6. https://doi.org/10.1115/1.2979795.

Iliescu, D., Schulson, E.M., 2002. Brittle compressive failure of ice: Monotonic versus cyclic loading. Acta Mater. 50, 2163–2172. https://doi.org/10.1016/S1359-6454(02)00060-5.

International Standard Organization, 2019. ISO 19906 Petroleum and Natural Gas Industries - Arctic Offshore Structures.

Jefferies, M.G., Wright, W.H., 1988. Dynamic response of Molikpaq to ice-structure interaction. In: Proc. 7th Int. Conf. Offshore Mech. Arct. Eng. IV, pp. 201–220.

Jones, S.J., 2007. A review of the strength of iceberg and other freshwater ice and the effect of temperature. Cold Reg. Sci. Technol. 47, 256–262. https://doi.org/10.1016/j.coldregions.2006.10.002.

Jordaan, I, O'Rourke, B., Turner, J., Moore, P., Ralph, F., 2016. Estimation of ice loads using mechanics of ice failure in compression. In: Arctic Technology Conference 2016. OTC (ATC). St. John's, Newfoundland and Labrador, Canada, pp. 1–12. https://doi.org/10.4043/27387-ms.

Jordaan, I.J., 2001. Mechanics of ice-structure interaction. Eng. Fract. Mech. 68, 1923–1960. https://doi.org/10.1016/S0013-7944(01)00032-7.

Jordaan, I.J., Stone, B.M., McKenna, R.F., Fuglem, M.K., 1992. Effect of microcracking on the deformation of ice. Can. Geotech. J. 29, 143–150. https://doi.org/10.1139/t92-015.

Kärnä, T., Kamesaki, K., Tsukuda, H., 1999. Numerical model for dynamic ice-structure interaction. Comput. Struct. 72, 645–658. https://doi.org/10.1016/S0045-7949(98)00337-X.

Kärnä, T., Jochmann, P., Kolari, K., 2001. Observed Ice - Structure Interactions in Winters 2000 and 2001 (No. STRICE D-3.1-A1), 1. Hamburg, Germany.

Korzhavin, K.N., 1962. Action of Ice on Engineering Structures. Publishing House of Siberian Branch of USSR Academy of Sciences.

Määttänen, M., 1988. Ice-Induced Vibrations of Structures - Self-Excitation, in: Proceedings of the 9th IAHR International Symposium on Ice. IAHR, Sapporo, Japan, pp. 658–665.

Matlock, H., Dawkins, W.P., Panak, J.J., 1969. A Model for the Prediction of Ice-Structure Interaction, in: Proceedings of the Annual Offshore Technology Conference. OTC, Dallas, Texas, USA, pp. 687–694. https://doi.org/10.4043/1066-ms.

Meglis, I.L., Melanson, P.M., Jordaan, I.J., 1999. Microstructural change in ice: II. Creep behavior under triaxial stress conditions. J. Glaciol. 45, 438–448. https://doi.org/10.3189/s0022143000001271.

Melanson, P.M., Meglis, I.L., Jordaan, I.J., Stone, B.M., 1999. Microstructural change in ice: I. Constant-deformation-rate tests under triaxial stress conditions. J. Glaciol. 45, 417–422. https://doi.org/10.3189/s0022143000001271.

Mellor, M., Cole, D.M., 1983. Stress/strain/time relations for ice under uniaxial compression. Cold Reg. Sci. Technol. 6, 207–230. https://doi.org/10.1016/0165-232X(83)90043-5.

Michel, B., Toussaint, N., 1977. Mechanisms and theory of indentation of ice plates. J. Glaciol. 19, 285–300.

Murdza, A., Schulson, E.M., Renshaw, C.E., 2020. Strengthening of columnar-grained freshwater ice through cyclic flexural loading. J. Glaciol. 66, 556–566. https://doi.org/10.1017/jog.2020.31.

Murdza, A., Schulson, E.M., Renshaw, C.E., 2021. Behavior of saline ice under cyclic flexural loading. Cryosph. 15, 2415–2428. https://doi.org/10.5194/tc-15-2415-2021.

Murdza, A., Schulson, E.M., Renshaw, C.E., Polojärvi, A., 2022. Rapid Healing of thermal Cracks in Ice. Geophys. Res. Lett. 49, 1–6. https://doi.org/10.1029/2022GL099771.

Owen, C.C., Hendrikse, H., 2023. An initial study of interference coloration for quantifying the texture and fabric of ice. Cold Reg. Sci. Technol. 206, 103735 https://doi.org/10.1016/j.coldregions.2022.103735.

Owen, C.C., Hammer, T.C., Hendrikse, H., 2022. Test setup for compressive loading of confined ice thick sections viewed with in-situ cross-polarization imaging. In: Proceedings of the 26th IAHR International Symposium on Ice. IAHR, Montréal, Canada, pp. 1–10.

Palmer, A., Qianjin, Y., Fengwei, G., 2010. Ice-induced vibrations and scaling. Cold Reg. Sci. Technol. 60, 189–192. https://doi.org/10.1016/j.coldregions.2009.11.005.

Peternell, M., Russell-Head, D.S., Wilson, C.J.L., 2011. A technique for recording polycrystalline structure and orientation during in situ deformation cycles of rock analogues using an automated fabric analyser. J. Microsc. 242, 181–188. https://doi.org/10.1111/j.1365-2818.2010.03456.x.

Peyton, H.R., 1968. Sea ice forces. In: Proceedings of Conference on Ice Pressures Against Structures, pp. 117–123.

Ravi-Chandar, K., Adamson, B., Lazo, J., Dempsey, J.P., 1994. Stress-optic effect in ice. Appl. Phys. Lett. 64, 1183–1185. https://doi.org/10.1063/1.110883.

Ren, S., Mazière, M., Forest, S., Morgeneyer, T.F., Rousselier, G., 2017. A constitutive model accounting for strain ageing effects on work-hardening. Application to a C–Mn steel. Compt. Rend. Mécan. 345, 908–921. https://doi.org/10.1016/j.crme.2017.09.005.

Rist, M.A., Murrell, S.A., 1994. Ice triaxial deformation and fracture. J. Glaciol. 40, 305–318. https://doi.org/10.3189/s0022143000007395.

Schulson, E., 1990. The brittle compressive fracture of ice. Acta Metall. Mater. 38, 1963–1976. https://doi.org/10.1016/0956-7151(90)90308-4.

Schulson, E.M., Duval, P., 2009. Creep and Fracture of Ice. Cambridge University Press. https://doi.org/10.1017/CBO9780511581397

Schulson, E.M., Gies, M.C., Lasonde, G.J., Nixon, W.A., 1989. The effect of the specimen-platen interface on internal cracking and brittle fracture of ice under compression: high-speed photography. J. Glaciol. 35, 378–382. https://doi.org/10.3189/S0022143000009308.

Schulson, E.M., Murdza, A., Renshaw, C.E., 2019. Mechanisms of Cyclic Strengthening and Recovery of Polycrystalline Ice, IUTAM Bookseries. Springer International Publishing, Espoo, Finland. https://doi.org/10.1007/978-3-030-80439-8_1.

Schwarz, J., 1994. Low Level Ice Forces, in: Proceedings of the 12th IAHR International Symposium on Ice. IAHR, Trondheim, Norway, pp. 1040–1050.

Sinha, N.K., 1989. Microcrack-enhanced creep in polycrystalline material at elevated temperature. Acta Metall. 37, 3107–3118. https://doi.org/10.1016/0001-6160(89)90346-5.

Sodhi, D.S., 1988. Ice-Induced Vibrations of Structures, in: Proceedings of the 9th IAHR International Symposium on Ice. IAHR, Sapporo, Japan, pp. 625–657.

Sodhi, D.S., 1991. Ice-structure interaction during indentation tests. In: Jones, S., McKenna, R.F., Tillotson, J., Jordaan, I. (Eds.), Proceedings of the IUTAM-IAHR Symposium on Ice-Structure Interaction. Springer-Verlag Berlin Heidelberg, St. John's, Newfoundland, Canada, pp. 619–640. https://doi.org/10.1007/978-3-642-84100-2_31.

Sodhi, D.S., 2001. Crushing failure during ice-structure interaction. Eng. Fract. Mech. 68, 1889–1921. https://doi.org/10.1016/S0013-7944(01)00038-8.

Sodhi, D.S., Haehnel, R.B., 2003. Crushing ice forces on structures. J. Cold Reg. Eng. 17, 153–170. https://doi.org/10.1061/(ASCE)0887-381X(2003)17:4(153).

Stone, B.M., Jordaan, I.J., Xiao, J., Jones, S.J., 1997. Experiments on the damage process in ice under compressive states of stress. J. Glaciol. 43, 11–25. https://doi.org/10.1017/S002214300000277X.

Szabo, D., Schneebeli, M., 2007. Subsecond sintering of ice. Appl. Phys. Lett. 90, 151916 https://doi.org/10.1063/1.2721391.

Timco, G.W., 1987. Indentation and penetration of edge-loaded freshwater ice sheets in the brittle range. J. Offshore Mech. Arct. Eng. 109, 287–294. https://doi.org/10.1115/1.3257022.

Toyama, Y., Sensu, T., Minami, M., Yashima, N., 1983. Model tests on ice-induced self-excited vibration of cylindrical structures. In: Proceedings of the International Conference on Port and Ocean Engineering under Arctic Conditions. Helsinki, Finland, pp. 834–844.

Tuhkuri, J., 1995. Experimental observations of the brittle failure process of ice and ice-structure contact. Cold Reg. Sci. Technol. 23, 265–278. https://doi.org/10.1016/0165-232X(94)00018-S.

Wachter, L.M., Renshaw, C.E., Schulson, E.M., 2009. Transition in brittle failure mode in ice under low confinement. Acta Mater. 57, 345–355. https://doi.org/10.1016/j.actamat.2008.09.021.

Wei, M., Polojärvi, A., Cole, D.M., Prasanna, M., 2020. Strain response and energy dissipation of floating saline ice under cyclic compressive stress. Cryosph. 14, 2849–2867. https://doi.org/10.5194/tc-14-2849-2020.

Wei, M., Prasanna, M., Cole, D.M., Polojärvi, A., 2022. Response of dry and floating saline ice to cyclic compression. Geophys. Res. Lett. 49, 1–10. https://doi.org/10.1029/2022GL099457.

Yap, K.T., 2011. Level Ice-Vertical Structure Interaction : Steady-State Self-Excited Vibration of Structures. National University of Singapore.